Resubmitted to the Journal of Sedimentary Research, April, 2005

# DEPOSITIONAL TURBIDITY CURRENTS IN DIAPIRIC MINIBASINS ON THE CONTINENTAL SLOPE: EXPERIMENTS - NUMERICAL SIMULATION AND UPSCALING

HORACIO TONIOLO[12], GARY PARKER[1], VAUGHAN VOLLER[1] AND R. T. BEAUBOUEF[3]

[1]*St. Anthony Falls Laboratory, University of Minnesota, Mississippi River at 3rd Ave. SE Minneapolis MN 55414 U.S.A.*
[2]*Now at University of Alaska Fairbanks, P.O. Box 755900, Fairbanks, AK 99775-5900 U.S.A.*
[3]*ExxonMobil Upstream Research Company, P.O. Box 2189, Houston, TX 77252 U.S.A.*

*e-mail: ffhat@uaf.edu, parke002@tc.umn.edu, volle001@tc.umn.edu, rick.t.beaubouef@exxonmobil.com*

KEY WORDS: diapirs, minibasins, turbidity currents, ponding, water detrainment, numerical model, hydraulic jump.

**ABSTRACT**: The northern continental slope of the Gulf of Mexico is riddled with numerous subsiding diapiric minibasins bounded by ridges, and often connected by channels created by turbidity currents. The region is economically relevant in that these diapiric minibasins constitute excellent focal points for the deposition of sand. These deposits in turn serve as excellent reservoirs for hydrocarbons. A better understanding of the "fill and spill" process by which minibasins fill with sediment as the intervening ridges are dissected by canyons may serve to aid in the location of such reservoirs. A theoretical analysis in a companion paper has revealed two key aspects of the "fill and spill" process; a) the formation of an internal hydraulic jump as a turbidity current spills into a confined basin, and b) the detrainment of water across a settling interface forming at the top of the ponded turbidity current downstream of the hydraulic jump. In that paper it was shown that sufficiently strong detrainment can consume the flow, so that there is no outflow of either water or sediment even with continuous inflow. As the basin fills with sediment, however, overspill is eventually realized. Herein the theory of the companion paper is used as the basis for a numerical model of ponding of turbidity currents. The numerical model is tested and verified against two experiments. In the first of these detrainment is sufficient to capture an entire sustained turbidity current. In the second of these detrainment is insufficient to prevent sustained overspill. The principles of similitude using the densimetric Froude number allow upscaling of the experimental results to field scale. A full numerical model is verified against the experiments and applied at field scale. The result is a view of intraslope minibasin sedimentation that has a stronger physical basis than the conceptual models proposed to date.

## INTRODUCTION

This paper presents a continuation of the analysis presented in a companion paper, Toniolo et al. (submitted). The focus of the both papers is the morphodynamics of the flow of turbidity currents and sediment deposition in diapiric minibasins such as those found on the northern continental slope of the Gulf of Mexico. The companion paper provides a theoretical analysis. In the present paper, a) the results of experiments are used to justify several key assumptions and conclusions of the theory of companion paper; b) the theory is augmented with a numerical model which is tested against the experimental results and c) the numerical model is applied at field scale.

The configuration studied here is one for which a turbidity current overspills the ridge between the minibasin of interest and the minibasin upstream, but before a canyon has been excavated into the ridge. As explained in the companion paper, Toniolo et al. (submitted), the overspilling turbidity current can be expected reach the Froude-critical condition at the apex of the ridge, and become supercritical as it flows down the slope into the minibasin. This configuration is outlined in Figure 6b of the companion paper, Toniolo et al. (submitted).

It is useful to elaborate upon the premises and results of the companion paper in the context of the configuration of the experiments reported in this paper. A simplified minibasin with a slot-like geometry and ending in a vertical wall with an overflow lip is illustrated in Figure 1. The minibasin has length $L_b$ and width $B_b$. A continuous, Froude-supercritical turbidity current driven by suspended sediment with a uniform grain size $D_s$ and corresponding fall velocity $v_s$ flows into the basin. The barrier at the downstream end forces ponding of the turbidity current. The zone of ponding is delineated by an internal hydraulic jump; it has length $L_p$. Upstream of the hydraulic jump the turbidity current is fully turbulent, and as it is Froude-supercritical it is able to entrain water from above. Downstream of the hydraulic jump the flow is slow and deep, with a densimetric Froude number well below unity (highly subcritical). The turbulence in the ponded zone is dying or dead, and settling is passive. The flow discharge, layer thickness, layer-averaged volume suspended sediment concentration and layer-averaged flow velocity are denoted as $Q$, $h$, $C$ and $U$; the corresponding inlet values at the upstream end of the basin are $Q_u$, $h_u$, $C_u$ and $U_u$.

The theoretical analysis indicates that the turbidity current forms a settling interface in the ponded zone downstream of the hydraulic jump. Water detrains across this interface, so weakening the turbidity current. If the surface area of the ponded zone is sufficient, all the water may detrain across the settling interface, so that there is no overflow over the downstream lip of the basin even with continuous inflow. In this case the minibasin captures 100% of the inflowing sediment. The theory predicts that the deposit thickness within the ponded zone should be spatially uniform. In addition, the concentration of suspended sediment should also be spatially uniform, and forward flow discharge should decrease linearly downstream in the ponded zone. As the sediment deposit builds up, the turbidity current should eventually overflow the basin.

The theoretical analysis of the companion paper has an essential drawback; it does not predict the position of the hydraulic jump. As a result it does not predict the length of the ponded zone $L_p$, and thus the detrainment discharge $Q_d$, = $v_s L_p B_b$. In addition, key assumptions of the theoretical analysis remain unjustified. These issues are resolved below.

## EXPERIMENTS

The results of two experiments (Experiments 1 and 3) carried out at St. Anthony Falls Laboratory, University of Minnesota are reported here. These experiments serve to a) verify the assumptions and some of the conclusions of the theory presented in the companion paper, Toniolo et al. (submitted) and b) provide data for a full numerical model of depositional turbidity currents in intra-slope minibasins.

The experimental facility consists of a flume that was specifically designed to allow the modeling of continuous turbidity currents extending for up to one hour (Garcia 1993). The flume is 0.304 m wide, 0.76 m deep and 12.80 m long, and has glass walls to facilitate flow visualization. The facility is equipped with a tank for the mixing of water-sediment slurries of specified concentration at the upstream end and a damping tank at the downstream end, as sketched in Figure 2. The damping tank plays a crucial role in the modeling of continuous turbidity currents. When a turbidity current reaches the invert at the damping tank, it falls into it and is sucked out from the bottom of the tank. The turbid water so lost is replaced by sediment-free water at the top of the tank; water surface elevation (base level) is maintained constant by means of a standpipe in the damping tank. As the turbidity current passes over the invert to the damping tank, its densimetric Froude number must become supercritical. This prevents reflection of the turbidity current and any information associated with it. As a result, continuous currents and their deposits can be studied without fear of pollution due to reflection from the downstream end.

Only a reach of 7 m toward the downstream end of the flume was used for the experiments. The basin of simplified geometry illustrated in Figure 3 was built in the flume. Its length $L_b$ = 4.06 m and its maximum relief $\Delta h_b$ = 0.46 m. The width $B_b$ of the minibasin was 0.304 m, i.e. the same as that of the flume. As can be seen in the figure, the model minibasin has an upstream region with a constant slope $S_{b1}$ = 0.298 (slope angle $\theta_{b1}$ = 16.6°), a nearly horizontal central region with slope $S_{b2}$ = 0.017 ($\theta_{b2}$ = 0.97) and a nearly vertical wall at the downstream end (Figures 1 and 3). In both Experiments 1 and 3 the water surface elevation $\xi_o$ measured relative to the lowest point of the initial bed (which was realized a the barrier; Figure 1) was held constant at 0.60 m.

The experimental configuration differs from those of natural diapiric minibasins in several ways. Firstly, the uniform width of the experimental configuration yields a slot-like 2D configuration. Most natural minibasins have more rounded 3D configurations, although some slot-like minibasins can be found in the field. Secondly, natural minibasins are not delineated by vertical walls at their downslope ends, but instead show a gradual increase in bed elevation toward a ridge (e.g. Hickson et al. 2000). It should be noted here that these simplifications to the configuration were selected to allow for testing of the theory and numerical model in the simplest and therefore most straightforward way. The theory itself is easily extendable to the case of 3D configurations with bowl-shaped rather than vertical confinement. Although the numerical model becomes rather more complicated, this too is in principle not difficult to extend to the 3D configuration. Finally, the present experiments are part of a larger program that includes experiments with more realistic downslope minibasin geometries (Hickson et al. 2000; Lamb et al. 2001) and an experiment in a subsiding 3D minibasin (Violet et al. 2001; Violet et al. in press).

The upstream mixing tank has a volume of 2000 liters. A propellor at the bottom keeps the water-sediment slurry fully mixed. A pump recirculates the slurry between the mixing tank and a much smaller constant-head tank above it. A dilute slurry is introduced to the flume from the constant-head tank. This allows the maintenance of nearly-constant slurry discharge into the flume even though the level the free surface of the slurry in the mixing tank continuously drops in time.

This tank was filled with fresh water and glass beads (ballotini) at a volume concentration of 5% in both Experiments 1 and 3. Experiment 2 was performed with the addition of salt to the glass beads and the water in the mixing tank. The salt was used to simulate a very fine grain size that would not settle out in the basin. The results of this experiment are not presented here because the extension of the theory presented here to the conditions of Experiment 2 is not yet complete.

The density $\rho_s$ of the glass beads (ballotini) used in the experiments was 2.50 g/cm$^3$. The beads were chosen so as to be as nearly uniform in size as possible. Grain size distribution varied slightly from batch to batch of purchased material. In the case of Experiment 1, the median size $D_{50}$ was 45 μm, the geometric mean size $D_g$ was 42 μm and the geometric standard deviation $\sigma_g$ was 1.25. In the case of Experiment 3, the median size was 47 μm, the geometric mean size was 46 μm and the geometric standard deviation was 1.25. The grain size distributions of the glass beads used in Experiments 1 and 3 are shown in Figure 4. The value of characteristic grain size $D_s$ used in the theory of the companion paper, Toniolo et al. (submitted) can be approximated with the observed value of $D_g$. Fall velocities $v_s$ for the sediment used in the experiments were computed based on the measured values of $D_g$ and sediment density and the relation of Dietrich (1982); the values are reported in Table 1. Deposits of the material formed during the experiments were found to have a porosity $\lambda_p$ near 0.45.

The slurry was discharged into the experimental minibasin through a submerged horizontal headgate that restricted the upstream flow thickness $h_u$ to 1 cm for the case of Experiment 1 and 2 cm for the case of Experiment 3. The bottom of the opening of the headgate was flush with the bottom of the flume, and the top was well below the water surface in the flume. The delivery rate of slurry from the mixing tank to the basin was controlled with a valve, and set to a specified value by means of repeated weighing of timed samples. The upstream flow discharges $Q_u$ for Experiments 1 and 3 was 0.33 liters/s and 1.90 liters/s, respectively, as reported in Table 1. In both experiments the flow at the inlet was supercritical in the sense of the densimetric Froude number $\boldsymbol{Fr}_d$, i.e. $\boldsymbol{Fr}_d > 1$, where

$$\boldsymbol{Fr}_d = \frac{U}{\sqrt{RgCh}} \tag{1}$$

In the above relation $g$ denotes the acceleration of gravity and $R$ denotes a submerged specific gravity of sediment, given as

$$R = \frac{\rho_s}{\rho} - 1 \tag{2}$$

where $\rho_s$ denotes sediment density and $\rho$ denotes water density. From the information in Table 1 it is found that the inlet values of $\boldsymbol{Fr}_d$ are 1.32 and 2.68 for Experiments 1 and 3, respectively.

Upon release from the headgate, the turbidity current formed a distinct front and migrated into the minibasin. The front eventually collided with the downstream barrier and ran up it a considerable distance, with some overflow in both experiments. The turbidity current reflected off the barrier to form an upstream-migrating bore, which eventually migrated upstream and stabilized to form an internal hydraulic jump. The turbidity current was strongly ponded downstream of the hydraulic jump.

The settling interface formed in the ponded zone was nearly horizontal, as shown in Figure 5. The interface is not as sharp as the one shown in Lamb et al. (2004), for example, because opaque quartz silica flour and kaolinite clay were employed in those experiments, whereas nearly transparent glass beads were employed in the present experiments. In the case of Experiment 1, the settling interface of the ponded zone equilibrated approximately 8 cm below the lip of the downstream barrier; in the case of Experiment 3 it equilibrated approximately 6 cm above it. The observation of an essentially horizontal settling interface in strongly ponded zone mediated by a barrier justifies one of the key assumptions of the companion paper, Toniolo et al. (submitted).

Measurements of suspended sediment concentration were performed in each experiment using 18 siphons. All but one of these siphons were members of one of three rakes in which they were stacked vertically, with one rake containing 5 siphons and the other two containing 6 siphons. This configuration allowed resolution of the vertical distribution of suspended sediment concentration. In each rake the separation between siphons was 1, 3, 4, and 12 cm in order from bottom to top for the four pairs associated with the bottom five siphons . The highest siphon in the two rakes with 6 siphons was located 12 cm above the one immediately below. These rakes were mounted on three carts distributed along the minibasin. The final siphon was located at the lip of the downstream end of the minibasin. It served to quantify the outflow of sediment from the basin. Samples from each of the siphons were taken at various times during the experiments. The sampling was done so as to yield samples from each siphon of each rake at a time that was as close as possible to the times at which the other samples were taken, so yielding a snapshot of the pattern of sediment suspension in the minibasin. These samples were later analyzed to obtain sediment concentrations and grain size distribution. The distributions were determined using an Elzone particle counter machine.

Fine coal was introduced to the turbidity current at the upstream end of the basin immediately after sampling was completed. The bed deposit was inscribed on the flume glass wall. Coal and inscriptions on the wall served to provide stratigraphic markers of bed elevation at the completion of sampling, as can be seen in Figure 6a.

Table 1 shows the discharge, duration, sampling time(s) (when siphon samples were taken) and bed marking time(s) for Experiments 1 and 3. The two discharges were selected based on many previous trial runs. The low discharge of Experiment 1 was selected specifically to model a turbidity current that would be completely captured in the minibasin despite continuous inflow. The substantially higher discharge of Experiment 3 was selected to model a turbidity current of sufficient strength to continuously overflow the minibasin. These estimates were performed in the following way. The length $L_p$ of the ponded zone was estimated as the length of the basin from the slope break to the mild slope $S_{b2}$ of 0.017 (Figure 3) to the barrier, i.e. 2.65 m. (This value is in fact an underestimate, as noted in Table 2 and discussed below). Using the formulation of the

companion paper (Toniolo et al.), the detrainment discharge $Q_d$ of water in the ponded zone, which is given as $Q_d = v_s B_b L$, was estimated from the fall velocities $v_s$ of Table 1 and the basin width $B_b$ of 0.304 m to be 1.13 liters/s in the case of Experiment 1 and 1.37 liters/s in the case of Experiment 3. Comparing these values with the inflow discharges $Q_u$ of Table 1, it is seen that $Q_u$ is considerably less than $Q_d$ in the case of Experiment 1 (allowing the possibility of complete capture of the turbidity current within the minibasin) and $Q_u$ is greater than the estimate of $Q_d$ in the case of Experiment 3 (indicating overflow of the turbidity current from the minibasin.)

The above estimates are not precise because a) the length of the ponded zone may not be precisely equal to the length from the slope break to the barrier in Figure 3 and b) the turbidity current may entrain water between the inlet and the hydraulic jump, so increasing its discharge. They nevertheless allowed for successful experimental design. At the end of Experiment 1 nearly all of the sediment was found to be captured within the minibasin (Figure 6a); the bed of the flume downstream of the minibasin was observed to be very nearly sediment-free (Figure 6b). The bed at the end of Experiment 3 is shown in Figure 7; a substantial deposit of sediment is seen downstream of the barrier.

During Experiment 1 shots of rhodamine dye were introduced in the turbidity current to improve the visualization of the internal hydraulic jump of Figure 1. Digital pictures were taken to document the jump. Although not shown here for the sake of brevity, the existence and position of the jump were clearly documented in this way.

After the experiments, the bed was profiled using a point gauge every 5.08 cm (2 inches) in the streamwise direction. In addition, the longitudinal variation in the grain size distribution of the deposit was characterized by means of 5 bed samples in Experiment 1 and 10 bed samples in Experiment 3. The bed elevation profiles and the cart positions for Experiments 1 and 3 are shown in Figures 8 and 9 respectively.

The images of Figures 6 and 7 and bed profiles of Figures 8 and 9 justify one of the conclusions of the theory of the companion paper, Toniolo et al. (submitted). In both experiments the hydraulic jump stabilized at a location not far from the bed slope break from the steeper slope $S_{b1}$ to the milder slope $S_{b2}$ evident in Figure 1 (and Figures 7 and 8 as well). It is seen in Figures 7 and 8 that ponding resulted in the formation of a sediment deposit that was nearly uniform in thickness in the downstream zone within the ponded zone, as predicted by the theory.

In the case of Experiment 1, which had a duration of 58 minutes, vertical profiles of volume sediment concentrations were collected at t = 16, 38, and 58 minutes. These profiles presented in Figures 10a – 10c; the positions of the siphon rakes are shown in Figure 8. In the case of Experiment 3, which had a duration of 11 minutes (due to the much larger flow discharge), corresponding profiles were collected at t = 8 minutes. These profiles are presented in Figure 11; the positions of the siphon rakes are shown in Figure 9.

In Experiment 1 the samples from the rake farthest upstream in Figures 10a, b, and c show profiles of suspended sediment that decay roughly exponentially in the vertical upward direction, a pattern that locates them upstream of the hydraulic jump (Garcia and Parker 1989). The other two rakes were positioned in the ponded zone. For these rakes, in all cases the vertical distribution of suspended sediment concentration was found to be approximately uniform in the vertical. The only deviation was at the uppermost siphon of Figures 10b and 10c, where the modest dip in concentration denotes

proximity to the interface between the sediment laden water below and the (nearly) clear water above. The fact that the grain size distribution was not absolutely uniform guaranteed the existence of a small amount of very fine sediment above an otherwise clear settling interface.

A comparison of the two profiles downstream of the jump in Figures 10a – 10c lead to a further conclusion; within the ponded zone, the suspended sediment concentration is not only approximately constant in the vertical up to the settling interface, but it is also approximately constant in the streamwise direction as well.

The positions of the siphon rakes for Experiment 3 are shown in Figure 9; the measured concentration profiles are shown in Figure 11. All the siphons in Experiment 3 were positioned after the hydraulic jump. In this case the settling interface was well above the uppermost siphon; the measured concentration profiles are strongly uniform in both the vertical and the streamwise direction.

Figures 10 and 11 thus serve to justify another of the key assumptions of the companion paper, Toniolo et al (submitted); in the ponded zone the sediment is well-mixed up to a relatively sharp settling interface. The approximation used by Toniolo et al. (submitted), according to which suspended sediment concentration in the ponded zone below the settling interface is equal to a constant, is supported by the data of both Experiments 1 and 3.

Figures 12 and 13 show plots of the vertical distributions of the geometric mean size obtained from the siphon samples in Experiments 1 and 3, respectively. The vertical variation of the geometric mean size again shows uniformity in the vertical. This result is largely a consequence of the low geometric standard deviation of the sediment used in the experiments.

Figures 14 and 15 show long profiles of the grain sizes associated with the peaks of the probability densities of size for the bed deposits at the end of Experiments 1 and 3, respectively. The peaks are used in preference to the geometric means due to the presence of small but unrealistic anomalies in the tails of the measured probability densities. Both experiments display a bed material with little downstream variation in characteristic grain size within the minibasin. Figure 15 shows that the sediment deposited downstream of the minibasin in Experiment 3 was somewhat finer than that deposited within the minibasin.

Figures 16 and 17 document an essential result of the experiments. In Figure 16 the interface between the turbid water below and the clear water above is clearly seen to be below the lip of the downstream end of the minibasin in the case of Experiment 1. The water above the interface is not completely clear due to pollution of the ambient water with a very low concentration of the finest sizes in the sediment. In order to document any sediment overflow, the concentration of sediment in the water at point located 4 cm above the lip of the downstream barrier was measured with a siphon. In the case of Experiment 1, these values are reported in Figures 10a - 10c. The sediment concentration above the lip is seen to be about 1/25 of that in the ponded zone of the minibasin. In addition, a) the injection of dye revealed no turbidity current spilling over the lip, and b) the bed downstream of the lip was observed to be almost completely free of visible sediment deposits at the end of the run, as documented in Figure 6b. Experiment 1 thus demonstrates the near-complete capture of a turbidity current in a minibasin, with almost no outflow of either water or sediment by means of a turbidity

current, even for a flow sustained over 58 minutes. Evidently water detrainment in the ponded zone was sufficient to accomplish this capture.

Figure 17, on the other hand, documents a substantial turbid underflow passing over the lip of the downstream end of the basin in Experiment 3. This is confirmed in Figure 11, which shows a sediment concentration just above the lip that is 80% of that observed in the ponded zone upstream. It can be inferred here that while water detrainment acted to sap the strength of the turbidity current in Experiment 3 as well, its effect was not strong enough to prevent significant outflow, or spill from the minibasin. The key difference between Experiments 1 and 3 leading to such different behavior is the upstream flow discharge of the turbidity current, which was much larger in the latter case.

Summarizing then, the experiments validate all three of the assumptions of the companion paper, Toniolo et al. (submitted): a) a downstream barrier can force a hydraulic jump to a strongly ponded flow with a nearly horizontal settling interface; b) the sediment is well-mixed in the vertical and streamwise directions in the ponded zone up to the settling interface, and c) the entire sustained turbidity current can be captured if the detrainment discharge of water is sufficiently high relative to the inflow discharge. In addition, the experiments verify one of the conclusions of the companion paper, i.e. that the deposit in the ponded zone should be of uniform thickness.

The theoretical model of the companion paper, Toniolo et al. (submitted) does, however, have one drawback. It is not capable of predicting the location of the hydraulic jump necessary to set up ponding of the current, nor is it capable of predicting how this location should evolve in time. For this purpose it is necessary to have a full numerical model. Such a model is delineated below.

## GOVERNING EQUATIONS OF THE NUMERICAL MODEL

The theoretical model presented in the companion paper, Toniolo et al. (submitted) is based on the concept of quasi-steady flow. That is, the model assumes that the flow adjusts rapidly to changing conditions, but the boundary adjusts much more slowly as sediment deposits from suspension. The formulation can be expected to be accurate as long as the turbidity current is sufficiently dilute. It is, however, insufficient to specify either the location of the hydraulic jump at the upstream end of the ponded zone or the setup to quasi-steady flow.

In the numerical model presented here the quasi-steady assumption is not employed. Instead, a shock-capturing technique is used so that the position and strength of the hydraulic jump can be solved simultaneously with all other unknowns. The numerical model is based on the layer-integrated formulation of Parker et al. (1986), but is modified to capture the effect of water detrainment across the interface between muddy water and clear water above. It solves a set of layer-integrated equations of flow continuity, momentum, sediment conservation along with the Exner equation of bed sediment conservation.

The original relations of Parker et al. (1986) take the forms

$$\frac{\partial h}{\partial t}+\frac{\partial Uh}{\partial x}=e_w U$$
$$\frac{\partial Ch}{\partial t}+\frac{\partial UCh}{\partial x}=v_s(E_s-r_o C)$$
$$\frac{\partial Uh}{\partial t}+\frac{\partial U^2 h}{\partial x}=-\frac{1}{2}Rg\frac{\partial Ch^2}{\partial x}+RgChS-C_{f0}U^2 \qquad (3a,b,c,d)$$
$$(1-\lambda_p)\frac{\partial \eta}{\partial t}=-v_s(E_s-r_o C)$$

where $x$ denotes streamwise distance, $t$ denotes time, $h$ denotes layer thickness of the turbidity current, $U$ denotes layer-averaged flow velocity, $C$ denotes layer-averaged volume concentration of suspended sediment, $\eta$ denotes bed elevation, $g$ denotes the acceleration of gravity, $S$ denotes bed slope, $C_{f0}$ denotes the coefficient of bed friction and $\lambda_p$ denotes the porosity of the bed deposit. The bed slope $S$ is related to bed elevation $\eta$ as

$$S=-\frac{\partial \eta}{\partial x} \qquad (4)$$

In Equation 3a $e_w$ denotes a dimensionless coefficient of entrainment of clear water from above into the turbidity current. In Equations 3b and 3d $E_s$ denotes a dimensionless coefficient of entrainment of bed sediment into the turbidity current and $r_o$ denotes a coefficient relating a near-bed concentration of suspended sediment to the layer-averaged value $C$. Equations 3a, 3b, 3c and 3d denote conservation equations for flow mass, suspended sediment, flow momentum, and bed sediment, respectively.

The derivation of Equations 3a – 3c are given in the Appendix of Parker et al. (1986). This derivation, however, applies to a fully turbulent turbidity current, and does not take into account the possibility of a ponded, turbidity current with a very low Froude number in which turbulence is dead or dying, which is bounded by a relatively sharp, turbulence-free settling interface at the top and from which sediment settles passively from suspension without any resuspension. As shown in the companion paper, the versions of Equations 3a – 3d applicable to this case are

$$\frac{\partial h}{\partial t}+\frac{\partial Uh}{\partial x}=-v_s$$
$$\frac{\partial Ch}{\partial t}+\frac{\partial UCh}{\partial x}=-v_s C$$
$$\frac{\partial Uh}{\partial t}+\frac{\partial U^2 h}{\partial x}+Uv_s=-\frac{1}{2}Rg\frac{\partial Ch^2}{\partial x}+RgChS-(C_{f0}+C_{fI})U^2 \qquad (5a,b,c,d)$$
$$(1-\lambda_p)\frac{\partial \eta}{\partial t}=-v_s C$$

Before proceeding, it is useful to compare Equations 3a – 3d with 5a – 5d.

Equations 3a and 5a describe the conservation of flow mass. In Equation 3a it is implicitly assumed that turbulence at the interface between muddy water and clear water above has destroyed any settling interface. In addition, clear water is entrained by turbulence into the turbidity current in accordance with the coefficient of water

entrainment $e_w$, which is in general assumed to be a function of the bulk Richardson number $\boldsymbol{Ri}$;

$$e_w = e_w(\boldsymbol{Ri})$$

$$\boldsymbol{Ri} = \frac{RgCh}{U^2} \tag{6a,b}$$

The parameter $\boldsymbol{Ri}$ is in turn related to the densimetric Froude number $\boldsymbol{Fr}_d$ as

$$\boldsymbol{Ri} = \frac{1}{\boldsymbol{Fr}_d^2} \tag{7}$$

An example of a relation for $e_w$ is that given in Parker et al. (1986);

$$e_w = \frac{0.00153}{0.0204 + \boldsymbol{Ri}} \tag{8}$$

from which it is easily established that $e_w \rightarrow 0$ as $\boldsymbol{Ri} \rightarrow \rightarrow\infty$ and thus $\boldsymbol{Fr}_d \rightarrow 0$. Thus Equation 3a correctly represents the vanishing of entrainment of water from above in a strongly ponded turbidity current for which $\boldsymbol{Fr}_d << 1$, but does not track the settling interface. Equation 5a both tracks the settling interface and allows water detrainment across it.

Equations 3b and 5b describe the conservation of suspended sediment, and Equations 3d and 5d describe the conservation of bed sediment. The latter equations are obtained from the respective former equations as $E_s \rightarrow 0$ and $r_o \rightarrow 1$. These limits reflect a) the inability of the dying turbulence to entrain sediment into suspension from the bed of a strongly ponded flow and b) the establishment of a profile of suspended sediment that is relatively uniform in the vertical due the mixing of the hydraulic jump.

Equations 3c and 5c describe the conservation of the momentum of the flow. They differ in that Equation 5c a) describes the tendency of the turbidity current to detrain forward momentum as it detrains water, and b) includes the possibility of interfacial friction at the sharp settling interface between muddy and clear water. Neither of these terms, however, can be expected to be very important in the case of a slowly moving, strongly ponded turbidity current containing relatively fine sediment.

In principle one can expect a smooth transition from Equations 3a – 3d to Equations 5a – 5d as the regime of unponded supercritical, fully turbulent turbidity currents devolves into the range of strongly ponded, highly subcritical turbidity currents in which the turbulence is dying. The derivation of such a set of equations is beyond the scope of the present analysis. Instead, the following set of equations is used to describe the experiments reported here;

$$\frac{\partial h}{\partial t} + \frac{\partial Uh}{\partial x} = (1-\delta)e_w U - \delta v_s$$

$$\frac{\partial Ch}{\partial t} + \frac{\partial UCh}{\partial x} = -v_s C$$

$$\frac{\partial Uh}{\partial t} + \frac{\partial U^2 h}{\partial x} + \delta U v_s = -\frac{1}{2} Rg \frac{\partial Ch^2}{\partial x} + RgChS - C_{f0} U^2 \tag{9a,b,c,d}$$

$$(1-\lambda_p)\frac{\partial \eta}{\partial t} = -v_s C$$

where $\delta$ is a parameter equal to unity in the ponded zone (where it is expected that $\boldsymbol{Fr}_d << 1$) and zero and the supercritical, turbulent zone upstream of the hydraulic jump. The

forms of Equations 9b and 9d reflect the fact that in the experiments reported here the turbidity currents were essentially purely depositional even in much of the turbulent zone upstream of the hydraulic jump. Such behavior should not necessarily be the case in the field.

## NUMERICAL SCHEME

The numerical solution proceeds in two parts; a) a solution of Equations 9a, 9b and 9c for the flow over a known bed, and b) a solution of Equation 9d for the modification of the bed resulting from this flow.

Equations 9a – 9c are in conservative form (Tannehill et al. 1997) and as such are intrinsically shock-capturing. In the context of the present work, this means that when implemented numerically, the positions of any hydraulic jumps or bores (which may be thought of as rapidly migrating jumps) are automatically captured.

The MacCormack scheme (MacCormack 1969; Tannehill et al. 1997) is used to solve the governing equations. This explicit scheme is second-order accurate both in space and time. Equations 9a – 9c may be written in compact vector form as

$$\frac{\partial A}{\partial t}+\frac{\partial B}{\partial x}=Z \tag{10}$$

in which

$$A=\begin{bmatrix} h \\ Ch \\ Uh \end{bmatrix} \tag{11}$$

$$B=\begin{bmatrix} Uh \\ CUh \\ U^2h+\frac{1}{2}RCgh^2 \end{bmatrix} \tag{12}$$

$$Z=\begin{bmatrix} (1-\delta)e_w U-\delta v_s \\ -Cv_s \\ RghCS-C_f U^2-\delta U v_s \end{bmatrix} \tag{13}$$

The MacCormack scheme comprises two parts, i.e. a predictor and a corrector. For the spatial derivatives, forward finite-difference approximations are used in the predictor part and backward finite-difference approximations are used in the corrector part. Let the index *i* refer to spatial steps and the index *k* refer to time steps. Where *k* refers to the current time step, the predictor takes the form

$$A_i^* = A_i^k - \lambda_M\left(B_{i+1}^k - B_i^k\right)+\Delta t Z_i^k \tag{14}$$

and the corrector takes the form

$$A_i^{**} = A_i^* - \lambda_M\left(B_i^* - B_{i-1}^*\right)+\Delta t Z_i^* \tag{15}$$

so that the value of *A* one time step later is given as

$$A^{k+1}=\frac{1}{2}(A^k + A^{**}) \tag{16}$$

In the above relations $\lambda_M = \Delta t / \Delta x$, the superscript asterisk (*) refers to the predicted value and the superscript double asterisk (**) refers to the correction.

Oscillations near steep gradients in the solution are damped using the form for artificial viscosity given by Jameson et al. (1981) (e.g. Gharangik and Chaudry 1991). Parameters $\varepsilon_i$ and $\varepsilon_{i+(1/2)}$ are first obtained from the computed flow depths as

$$\varepsilon_i = \frac{\left|h_{i+1} - 2h_i + h_{i-1}\right|}{\left|h_{i+1}\right| + 2\left|h_i\right| + \left|h_{i-1}\right|} \tag{17}$$

$$\varepsilon_{i+(1/2)} = \kappa \frac{\Delta x}{\Delta t} \max(\varepsilon_{i+1}, \varepsilon_i) \tag{18}$$

where the parameter $\kappa$ is used to regulate the amount of artificial dissipation. The computed variables are then modified according to the formulation

$$f_i^{k+1} = f_i^{k+1} + \varepsilon_{i+(1/2)}(f_{i+1}^{k+1} - f_i^{k+1}) - \varepsilon_{i-(1/2)}(f_i^{k+1} - f_{i-1}^{k+1}) \tag{19}$$

After the variables at the new time step are computed according to Equation 19, Equation 9d is solved to update the bed profile. The time step Δt is chosen to as to satisfy the appropriate stability condition for the MacCormack scheme;

$$\Delta t \le C_n \frac{\Delta x}{\max(\left|U\right| + \sqrt{gh})} \tag{20}$$

in which $C_n$ is the Courant number, which must be less than or equal to 1.0 for this scheme.

The equations must be solved with appropriate initial and boundary conditions. The long-term morphodynamics of the minibasin are independent of the initial conditions of the flow, and as a result these are chosen mostly for convenience. For the initial conditions, the flow at time *t = 0* is assumed to be Froude-critical in the entire domain in the case of no overflow over the downstream lip, and Froude-subcritical under the condition of overflow at the downstream lip of the basin. The initial discharge is everywhere set equal to the product of the velocity and depth at the upstream end of the minibasin at time *t = Δt*. The initial volume concentration of suspended sediment is assumed to be very small ($<10^{-3}$) and constant over the whole domain.

The long-term morphodynamics of the basin are, however, critically sensitive to boundary conditions. In the numerical model flow thickness *h*, velocity *U* and concentration *C* must be specified at the node farthest upstream whether or not overflow at the downstream lip is considered. When a condition of no overflow is simulated, another boundary condition must be added. That is, the velocity at the node farthest downstream must be equal to 0. It is important to realize, however, that whether or not overflow occurs is dictated by the existing bed geometry, the water detrainment discharge and upstream boundary conditions. An imposition of zero velocity at the downstream end of a flow that would naturally overflow leads to an interface between the ponded muddy water and clear water that rises to the elevation of the downstream lip of the minibasin, at which point the model fails. In such a case the calculation must be repeated assuming overflow.

## NUMERICAL SIMULATION OF THE EXPERIMENTS

The numerical model was tested against the results of Experiments 1 and 3. The input parameters required by the model are the following: layer thickness $h_u$, layer-averaged velocity $U_u$ and layer-averaged volume sediment concentration $C_u$ of the turbidity current at the upstream end of the minibasin, initial basin bathymetry (i.e. geometry of the inerodible bed), water surface elevation, fall velocity of sediment $v_s$, submerged specific gravity of the sediment $R$, porosity of the sediment deposit $\lambda_p$ and bed friction factor $C_{f0}$ of the turbidity current. All of these parameters were measured directly except fall velocity $v_s$, which was computed from the relation of Dietrich (1982), and bed friction coefficient $C_{f0}$, which was matched to the data by trial and error.

The streamwise spatial increment $\Delta x$ used in the calculations was 2.54 cm. The time step $\Delta t$ was calculated at each time step according to Equation 20; it was on the order of $10^{-2}$ sec.

The turbidity current in Experiment 1 was purely depositional throughout the entire minibasin. This was evidenced by the way sediment draped over minor irregularities on the bed, such that the imprint of the irregularities was preserved in the vertical within the stratigraphy (Figure 6a). As a result data from the experiment could be applied directly as input data for the simulation. The friction factor $C_{f0}$ used in the simulation was 0.0069, a value that was determined by trial and error. The results of the simulation were not found, however, to be strongly dependent on the choice of $C_{f0}$**.** The model located the submerged hydraulic jump in the same place as was observed in the flume by means of flow visualization with rhodamine dye. Also, a condition of no overflow was verified both in experiment and numerical simulation. A comparison between experiment and model at time t = 16 minutes is shown in Figure 18. The agreement is excellent in the ponded zone beyond the hydraulic jump. It is worthwhile noting that the model failed to reproduce the draping over two irregularities on the bed visible in Figure 6a only because the initial bed profile used in the model was smoothed to remove them.

The time t = 16 minutes of Figure 18 is well beyond the time necessary to set up a quasi-steady flow with a hydraulic jump and settling interface that migrate only slowly in response to bed evolution. It should be noted, however, that the model also captures the setup to quasi-steady flow, including a) a turbidity current with a distinct front migrating toward the barrier, b) runup at the barrier and c) reflection in the form of a bore, the position of which eventually stabilizes as a hydraulic jump. All of these features are described for the case of Experiment 1 in Figure 19. It is seen in that figure that setup is nearly complete by 140 seconds after run commencement. The setup process, however, was too short to contribute much to the morphodynamic evolution of the bed shown in Figure 18 at 16 minutes.

The turbidity current in Experiment 3 was sufficiently strong that it kept the bed sediment-free for the first 10 cm downstream of the headgate. That is, the upstream part of the turbidity current was not purely depositional, and thus did not conform to one of the assumptions stated above. It was evident from the experiment, however, that the turbidity current became predominantly, and then exclusively depositional a short distance downstream. With this in mind, the numerical model was first used to simulate a conservative flow (i.e. one that neither deposits nor erodes sediment) from the headgate to a point farther downstream, beyond which it could be reasonably approximated as

predominantly depositional. That is, the upstream conditions for the depositional model were imposed at a point offset 25 cm from the headgate, using the values of $h_u$ and $U_u$ computed from the conservative model and the unmodified value of $C_u$. The results of the calculations are summarized in Figure 20. The agreement between the model and the experiment is excellent within the ponded zone downstream of the hydraulic jump. Some discrepancy still appears near the upstream end, but the reason for this is clear; the current was not purely depositional there, whereas the model is.

The numerical model was found to predict a location for the settling interface that was in good agreement with the data in the case of Experiment 1 and excellent agreement in the case of Experiment 3. The differences between the measured values of the elevation of the settling interface and those of the numerical simulation were approximately 3 cm and 1 cm in Experiments 1 and 3 respectively. It should be pointed out, however, that a very low concentration of the finest sediment in the initial mix was observed above the settling interface in Experiment 1, as can be seen in Fig. 16. This feature indicates the degree to which the approximation of completely uniform sediment fits the conditions of the experiment.

The good agreement between the numerical model and parameters that could easily be measured for the experiments (length and elevation of the ponded zone and thickness of the deposit at the end of the run) suggests that parameters which could not be measured during the experiments can be reasonable estimated from the numerical model. Several of these estimates are given in Table 2: the parameters are a) the flow discharge $Q_{bj}$, flow velocity $U_{bj}$, flow thickness $h_{bj}$, volume suspended sediment concentration $C_{bj}$, densimetric Froude number $\boldsymbol{Fr}_{dbj}$ and the ratio $U_{bj}/v_s$ where the subscript "*bj*" denotes just before the hydraulic jump; b) the corresponding parameters just after the hydraulic jump, denoted with the subscript "*aj*"; the length $L_p$ of the ponded zone and the detrainment discharge $Q_d$, given as Equation 2 in the companion paper, Toniolo et al. (submitted),and here as

$$Q_d = B_b L_p v_s \tag{21}$$

The estimates of Table 2 indicate that the flow was highly supercritical just before the jump (with $\boldsymbol{Fr}_d$ taking values of 4.02 and 4.13 for Experiments 1 and 3, respectively) and highly subcritical just after the jump (with $\boldsymbol{Fr}_d$ taking values of 0.042 and 0.049 for Experiments 1 and 3, respectively). These values are in correspondence with one of the assumptions of the theory presented in the companion paper: the barrier produces a hydraulic jump to highly subcritical, and thus highly ponded flow. In both experiments the flow discharges $Q_{bj}$ just before the jump are significantly higher than the corresponding inflow values $Q_u$, and the volume suspended sediment concentrations $C_{bj}$ just before the jump are significantly lower than the corresponding inflow values $C_u$ (compare Tables 1 and 2). This is because of water entrainment in the supercritical flow upstream of the jump. Table 2 also indicates that in the case of Experiment 1 the detrainment discharge $Q_d$ is slightly higher than the flow discharge $Q_{bj}$ just before the jump, whereas in Experiment 3 the detrainment discharge is lower than the flow discharge just before the jump. This is in correspondence with the observed result that in Experiment 1 the settling interface equilibrated below the lip of the barrier (resulting in nearly complete capture of the sustained turbidity current), whereas in Experiment 3 it equilibrated above it (resulting in significant sustained overflow).

Table 2 also indicates that in both experiments the ponded zone was longer than the length of the basin with low slope $S_{b1}$ (Figure 3). That is, ponding forced the hydraulic jump to occur upstream of the slope break.

Also listed in Table 2 are computed values for the ratios $U_{bj}/v_s$ and $U_{aj}/v_s$ for both experiments. The values just upstream of the jump, i.e. 158 for Experiment 1 and 266 for Experiment 3, correspond to flows that were observed to be nearly or completely depositional. The values just downstream of the jump, i.e. 7.5 and 14, are much lower, corresponding to the observed purely depositional flows in the ponded zone.

Note that in Table 2 the values for flow discharge $Q_{aj}$ and volume suspended sediment concentration $C_{aj}$ just after the jump are equal to their values $Q_{bj}$ and $C_{bj}$ just before the jump. This reflects the observation that internal hydraulic jumps are known to be ineffective at entraining ambient water into the underflow (Wilkinson and Wood 1971; Stefan and Hayakawa 1972; Baddour 1987). As a result, the flow is not diluted as it goes through the jump, and flow discharge and suspended sediment concentration do not change across it.

## COMPARISON OF THE THEORETICAL MODEL OF THE COMPANION PAPER AGAINST THE NUMERICAL MODEL

The theory of the companion paper, Toniolo et al. (submitted) provides four predictions in regard to the ponded zone of a sustained, fully ponded turbidity current in a slot-like basin of constant width with constant inflow (Equations 13b, 15, 19b and 22 of that paper). These predictions are repeated here for reference.

1. The elevation $\xi$ of the settling interface should be nearly horizontal, so that

$$\xi(x) = const \tag{22}$$

2. The volume concentration of suspended sediment $c$ should be constant in the vertical from the bed to the settling interface, and constant in the streamwise direction, so that the layer-averaged volume concentration of suspended sediment $C$ obeys the relation

$$C(x) = const \tag{23}$$

3. The forward flow discharge $Q$ declines linearly in the streamwise direction, so that where $Q_{aj}$ denotes the flow discharge at the upstream end of the ponded zone (immediately after the hydraulic jump),

$$Q = Q_{aj} - v_s B_b x \tag{24}$$

4. The sediment deposit has a uniform thickness in the streamwise direction, so that where $\eta(x,t)$ denotes bed elevation at streamwise location $x$ and time $t$, and $\eta_I(x)$ denotes antecedent bed elevation,

$$\eta(x,t) = \eta_I(x) + \frac{v_s C}{(1-\lambda_p)} t \tag{25}$$

The experimental results reported above provide direct confirmation of Equations 22, 23 and 25. The full numerical model confirms the predictions of Equations 22 ~ 25 as well. This is demonstrated in Figure 21.

## SCALEUP OF THE EXPERIMENTS TO FIELD SCALE

The two experiments reported here are not designed to model sedimentary processes in any particular field-scale minibasin. Models at laboratory scale can,

however, provide useful information concerning field-scale processes. This is illustrated here using undistorted Froude modeling.

Scale models based on the principles of similitude have a long history in the fields of aeronautics and river engineering (e.g. Ettema et al. 2000). A model provides an exact representation of a larger (or smaller) prototype if a) geometric similitude is maintained, so that every length scale in the prototype can be obtained by multiplying the corresponding length scale in the model by a constant scale ratio $\lambda$; and b) the relevant dimensionless numbers governing the dynamics of the flow and morphodynamics of the bed are the same in the prototype as they are in the model.

In the case of turbidity current morphodynamics, there are three relevant dimensionless parameters; 1) the densimetric Froude number (the square of which represents the ratio of inertial to gravitational forces), 2) the Reynolds number (which represents the ratio of inertial to viscous forces) and 3) an as-yet poorly-defined dimensionless number representing the erodibility of cohesive mud. Here the scaleup is performed under the assumption of non-cohesive sediment, so eliminating the need for similitude in the third parameter. Even in the case of non-cohesive sediment, however, relations involving the entrainment of sediment from the bed typically indicate a Reynolds dependence (e.g. Garcia and Parker 1993; Wright and Parker 2004). Here the need for similitude in the Reynolds number is removed by considering only a purely depositional, highly ponded turbidity current. In such a ponded zone, similitude can be maintained to a high degree of accuracy by imposing only geometric similitude and similitude in the densimetric Froude number.

The relation between grain size $D_s$ and fall velocity $v_s$ does involve a Reynolds dependence (e.g. Dietrich 1982). In the case of a purely depositional turbidity current, however, the parameter that enters directly into the morphodynamics of the problem is the fall velocity $v_s$, not the grain size $D_s$. As a result, the principles of Froude similitude can be applied to fall velocity $v_s$, and the equivalent grain size $D_s$ can then be calculated using a relation for fall velocity such as that of Dietrich (1982).

Now let $\ell'$ denote any relevant length scale, e.g. length of the minibasin or height of the downstream barrier. Geometric similitude requires that

$$(\ell')_p = \lambda(\ell')_m \tag{26}$$

where the subscripts "$p$" and "$m$" denote "prototype" and "model," respectively, and $\lambda$ denotes a specified constant scale ratio. (Densimetric) Froude similitude requires that

$$\left(\frac{u'}{\sqrt{Rgc'\ell'}}\right)_p = \left(\frac{u'}{\sqrt{Rgc'\ell'}}\right)_m \tag{27}$$

where $u'$, $c'$ and $\ell'$ are shorthand for any velocity, volume concentration of suspended sediment and length (as long as the model and prototype values correspond precisely to each other). In addition to Equations 26 and 27, the following scaling criterion is added here;

$$(c')_p = (c')_m \tag{28}$$

That is, the distribution of volume suspended sediment concentration is the same in the prototype as it is in the model. Application of Equations 26, 27 and 28 results in the following scale relations; where $Q'$ denotes any volume discharge and $t'$ denotes any time,

$$(\ell')_p = \lambda(\ell')_m \quad , \quad (u')_p = \lambda^{1/2}\sqrt{\frac{(R)_p}{(R)_m}}(u')_m$$
$$(Q')_p = \lambda^{5/2}\sqrt{\frac{(R)_p}{(R)_m}}(Q')_m \quad , \quad (t')_p = \sqrt{\frac{(R)_m}{(R)_p}}\lambda^{1/2}(t')_m \qquad (29a,b,c,d)$$

Equations 26 ~ 29 are applied to the results of Experiment 1 with a scale ratio $\lambda$ of 1000. The prototype sediment is assumed to have a specific gravity of 2.65, so that $(R)_p$ is equal to 1.65, as opposed to a model value $(R)_m$ of 1.50. Upscaling of measured parameters for Experiment 1 are given in Table 3; there $\boldsymbol{Fr}_{du}$ denotes the upstream value of the densimetric Froude number and $T_r$ denotes the duration of the experiment. (Upscaled values of parameters upstream of the ponded zone are provided for reference only; Froude similitude alone may not be sufficient there.) Upscaling of parameters for the ponded region of Experiment 1 predicted from the numerical model are given in Table 4. All prototype (field) parameters in Tables 3 and 4 were obtained from Equations 26 ~ 29 except sediment size $D_s$, which was computed from the prototype fall velocity $(v_s)_p$ computed according to Equation (29b) and the fall velocity relation of Dietrich (1982) assuming the appropriate value of $R$ and a kinematic viscosity of water $\nu$ of $1\text{x}10^{-6}$ $m^2/s$ (the clear water value for 20° C).

The scaleup corresponds to a prototype (field-scale) minibasin with a length $L_b$ of 4.06 km and a relief $\Delta h_b$ of 460 m created by a barrier These values are within the observed range for diapiric minibasins on the northern continental slope of the Gulf of Mexico (e.g. Lamb et al. 2004). The effective size of the sediment $D_s$ carried by the prototype current is 342 μm. The hydraulic jump induced by the barrier creates a ponded flow with a depth $h_{aj}$ just after the jump of 400 m. The flow velocity $U_{aj}$ and densimetric Froude number $\boldsymbol{Fr}_{aj}$ in the ponded zone just after the jump are 0.35 m/s and 0.042, respectively; both values decline to zero at the barrier, so indicating a highly ponded flow. The detrainment discharge $Q_d$ is 43,200 $m^3/s$, i.e. higher than the flow discharge $Q_{aj}$ of 42,500 $m^3/s$ just after the jump, so that no escape of the turbidity current would be expected. The volume sediment concentration $C_{aj}$ in the ponded zone is 0.011, indicating a dilute suspension.

The ratio $U_{aj}/v_s$ in the prototype ponded zone is 7.5, i.e. the same value as in the model. Even in the absence of a precise formulation for sediment entrainment, this value is low enough to suggest that the flow in the ponded zone should be incapable of re-entraining sediment as it settles out. The issue is explored in more detail below.

The following approximate threshold has been proposed by Bagnold (1966) for the onset of significant entrainment of bed sediment into suspension;

$$\frac{u_*}{v_s} = 1 \qquad (30)$$

where $u_*$ denotes shear velocity, which is related to the boundary shear stress $\tau_b$ at the bed and the layer-averaged flow velocity as

$$\tau_b = \rho u_*^2 = \rho C_{fo} U^2 \qquad (31)$$

where $C_{fo}$ is the dimensionless bed friction coefficient appearing in Equations 3c and 5c. Between Equations 30 and 31, the threshold for entrainment of sediment into suspension can be cast into the form

$$\frac{U}{v_s} = \frac{1}{\sqrt{C_{fo}}} \tag{32}$$

Estimating the friction coefficient for actively flowing field-scale turbidity currents as in the range 0.001 to 0.003 (e.g. Fukushima et al. 1985), Equation 32 indicates that $U/v_s$ should exceed a value between about 18 and 32 in order to entrain sediment from the bed. These thresholds are, however, likely to be too low for the case of a fully ponded current. More specifically, a current with a layer-averaged flow velocity of 0.35 m and a flow thickness of 400 m should generate so little shear at the bed that the effective friction coefficient should be much smaller. A crude way to estimate this effect is through the Parker (1991) form of the Manning-Strickler relation for bed resistance in a river, which takes the form

$$C_{fo} = 0.0152\left(\frac{h}{k_s}\right)^{-1/3} \tag{33}$$

where $k_s$ denotes a bed roughness height. (The estimate is crude because the flow in the ponded zone may not be hydraulic rough, may not even be turbulent, and may be associated with a boundary layer within the ponded zone that thickens downstream.) Estimating $k_s$ as equal to twice the characteristic size of the upscaled bed sediment for experiment 1, and estimating $h$ in terms of the upscaled values of $h_{bj}$ (just before the jump) and $h_{aj}$ (just after the jump), Equation 33 yields the estimates

$$C_{fobj} = 0.00108 \quad , \quad C_{foaj} = 0.000393 \tag{34a,b}$$

where again the subscripts "*bj*" and "*aj*" denote "just before the jump" and "just after the jump," respectively. Using equation 34b as a crude estimate for the ponded zone, then, the corresponding crude estimate for the onset of significant entrainment of bed sediment at prototype scale takes the form

$$\frac{U}{v_s} = 50 \tag{35}$$

This value supports the conclusion that a value of $U_{aj}/v_s$ of 7.5 is much too low for significant re-entrainment of sediment in the ponded zone.

The likely absence of sediment entrainment in the prototype ponded zone is not necessarily due to the the coarseness of the upscaled sediment, i.e. 342 μm. The calculation may be repeated using the same numbers as before except for grain size, which is reduced to 100 μm, corresponding to a fall velocity $v_s$ of 0.748 cm/s. The upscaled value of $U_{aj}/v_s$ is increased from 7.5 to 47 by the reduction in fall velocity, but the estimate of the value $U/v_s$ at the threshold for significant suspension is increased from 50 to 62. The analysis strongly suggests, then, the sediment entrainment would be absent in the ponded zone even with much finer sediment.

The estimates given above suggest that the bed friction coefficient $C_{fo}$ is very small in the ponded zone. In point of fact it was neglected in the theory of the companion paper, Toniolo et al. (submitted). A re-analysis of the results from the numerical simulations of Experiments 1 and 3 indicate that the calibrated value $C_{fo}$ of 0.0069 used in the simulations led to shear stresses in the ponded zone that have negligible effect on the results. (The effect upstream of the hydraulic jump is not negligible). The neglect of bed friction in the ponded zone is likely all the more accurate at field scale.

Thus the same ponding observed at laboratory scale in Experiment 1 is dynamically feasible at the scale of diapiric minibasins on the northern continental slope of the Gulf of Mexico. As long as the turbidity current is strong enough to reach the downstream end of the minibasin in the first place, the setup to and maintenance of a ponded flow should be similar to that described in the experiments here. The laboratory-scale hydraulic jump of Experiment 1 (and for that matter Experiment 3) was sufficient to mix 42 μm sediment essentially uniformly in the ponded zone up to the settling interface; dynamic similarity implies that the upscaled jump of Experiment 1 should be competent to do the same with 342 μm sediment at field scale.

Lamb et al. (2004) provide an estimator for the setup $T_s$ time to ponded flow after the front of the current has reached the barrier; the relation takes the form

$$T_s = \frac{L_b}{\sqrt{RgC\,\Delta h_{bo}}} \tag{36}$$

where $\Delta h_{bo}$ denotes the height of the bore as it migrates upstream after reflecting from the barrier. The height of the bore $\Delta h_{bo}$ in the case of Experiment 1 can be estimated from Figure 19 as 0.17 m; with $\lambda$ = 1000 this value upscales to 170 m. In addition, $C$ can be estimated using the value $C_{bj}$ of 0.011 just before the jump for Experiment 1, as given in Table 2. According to Equation 28, the corresponding upscaled value should be identical. The setup time $T_s$ is thus predicted to be 12.3 minutes. As long as the duration of flow is much longer than this time, the deposit from a given flow event will be predominantly the result of the ponded flow, not the setup to ponding.

The scaleup of sediment size from 42 μm to 342 μm of Table 3 implies a sand-rich turbidity current, carrying material that is likely toward the coarse end of the sand deposits observed in Gulf of Mexico minibasins. It should be noted, however, that this does not diminish the value of the experiments. The experiments offer a means to verify the numerical model, which can then be applied with more confidence at field scale using more typical values for sediment size and other parameters.

Having said this, it is of value to speculate concerning the type of deposit that would be created by the passive rainout of 342 μm sand in a ponded zone downstream of a hydraulic jump. If ponding is sufficiently strong the values of bed shear stress $\tau_b$ in the ponded zone can be expected to be too low to move, much less re-entrain the sand as it settles out. The result would be a thick, massive, structureless sand deposit. Such deposits have previously been inferred to have been created by "high-density turbidity currents" (e.g. Kneller and Branney 1995). A hydraulic jump to highly ponded flow provides an alternative mechanism by which a thick, massive sand deposit could also be created by a dilute turbidity current.

## NUMERICAL SIMULATION AT FIELD SCALE

As was illustrated in Figure 2 of the companion paper, Toniolo et al. (submitted), flow into diapiric minibasins on the northern continental slope of the Gulf of Mexico is often channelized into canyons incised into the ridges between basins. In principle, this erosion can be described in terms of an appropriate quantification of the parameter $E_s$ in Equations 3b and 3d. While the problem of channel erosion by turbidity currents is of considerable interest, it is beyond the scope of the present paper. This notwithstanding, an extension of the numerical model to field scale still serves a useful purpose, in that the

numerical model acts as a bridge between laboratory and field scale. The absence of a description of the entrainment of bed sediment in Equations 9b and 9d, however, ensures the prediction of a large, spurious rate of bed deposition in at least part of the steep, supercritical zone upstream of the hydraulic jump of Figure 1.

With this in mind, the following *ad hoc* formulation is used to characterize the supercritical zone of the turbidity current upstream of the hydraulic jump in an application of the numerical model to field scale. The zone of supercritical flow is forced to aggrade at precisely the same rate as the ponded zone, so that within that zone Equations 9b and 9d are modified to

$$\frac{\partial Ch}{\partial t} + \frac{\partial UCh}{\partial x} = -v_s C_p$$
$$(1-\lambda_p)\frac{\partial \eta}{\partial t} = -v_s C_p \qquad (37a,b)$$

where $C_p$ denotes the concentration of suspended sediment in the ponded zone. The implementation of Equations 9a, 9b (in the ponded zone), 37a (in the supercritical zone), 9c, 9d (in the ponded zone) and 37b (in the supercritical zone) must proceed iteratively so as to ensure that sediment continuity is satisfied. The formulation of Equations 37a and 37b, while still yielding sediment deposition in the supercritical zone, prevent the effect from overwhelming the calculation.

The minibasin is assumed to be 4500 m long, and have a width of 200 m. The initial bed profile of the minibasin has a break at 3000 m, such that the bed slope upstream and downstream of the break $S_{b1}$ is 0.05 and 0, respectively. The inflow discharge $Q_1$ at the upstream end of the minibasin is 200 $m^3/s$. This inflow is laden with a 2.5% volume concentration of 100 μm sediment. The sediment has a specific gravity of 2.65. The deposited sediment is assumed to have a porosity $\lambda_p$ of 0.6. The value of the bed friction coefficient $C_{fo}$ is taken to be 0.003. The basin is assumed to end in a vertical wall that is sufficiently high to prevent any overflow. Total run time is $4.3 \times 10^6$ seconds, or 49.8 days. The results should not be interpreted in terms of a continuous flow lasting for nearly 50 days, but rather in terms of the composite of intermittent flow events, each with a duration of tens of minutes, hours or possibly a few days.

The predictions of the model are described in Figures 22a – 22d. Figure 22a shows the evolution of the bed profile in time. Figure 22b shows the evolution of the interface between turbid and clear water, including the hydraulic jump. It should be noted that this interface can be expected to be quite diffuse in the supercritical zone, but relatively sharp in the ponded zone. Figure 22c shows the streamwise variation in flow discharge at the end of the run. Note that flow discharge increases dramatically, i.e. 18 fold in the supercritical zone due to water entrainment, and decreases equally dramatically in the ponded zone due to water detrainment. The spike at the hydraulic jump is an artifice of the numerical method, and is not real. The downstream variation in sediment discharge is shown in Figure 22d; note that all the sediment is captured in the minibasin. Again, the spike at the hydraulic jump in Figure 19d is an artifice of the numerical method and should be ignored.

The field-scale calculation illustrates two points; a) the flow discharge of a supercritical turbidity current can increase dramatically in the downstream direction due to water entrainment, and b) ponding and water detrainment is an effective way to capture sediment within a minibasin. The precise details of the calculation upstream of

the hydraulic jump are not intended to be an accurate model of nature, because in this steep zone bed erosion, or at least the suppression of deposition due to resuspension of sediment can be expected.

## DISCUSSION

The single most important result of this paper is the experimental verification of the theoretical conclusion presented in the companion paper, Toniolo et al. (submitted), that it is possible for a turbidity current to flow continuously into a minibasin and yet produce no outflow whatsoever due to the effect of water detrainment. As has been seen in the companion paper, the potential detrainment discharge associated with minibasins in the field is huge. Depending on grain size, it can range from tens of thousands to hundreds of thousands of cubic meters per second.

The results of the present paper as well as those of the companion paper, Toniolo et al. (submitted) raise a number of issues that merit further discussion. These issues are addressed below in the context of replies to rhetorical questions.

**Must the inflow to the minibasin always be supercritical?** The case of interest here is that of unchannelized spill over a ridge into an as-yet unfilled minibasin, as sketched in Figure 6b of the companion paper, Toniolo et al. (submitted). Under the conditions of that figure, the turbidity current at the crest of the ridge must be critical, and the flow farther downstream must be supercritical.

There are two cases for which subcritical flow into a minibasin can occur. The first of these is when a canyon has been excavated into the ridge between the minibasin of interest and the one immediately upstream, so that the downstream bed slope in the canyon differs little from that in the minibasin itself. Such a configuration eventually evolves in the field; it is described in Figures 2b and 2c in the companion paper, Toniolo et al. (submitted). The configuration of interest in the present paper is, however, one for which a canyon has not yet been excavated into the ridge upstream.

The second case for which the flow into the minibasin could be subcritical is when the turbidity current is so thick that the hydraulic control at the ridge is drowned out. This issue is most easily explored by means of analogy to open channel flow. Consider the steady, uniform Froude-subcritical flow in an open channel sketched in Figure 23a. In Figure 23b the flow has the same discharge, and the bed has the same mean slope as Figure 23a, but a periodic undulation in bed elevation is imposed. As long as the amplitude of the bed undulation is not very high, the flow remains Froude-subcritical everywhere; the flow accelerates slightly over the elevation highs and decelerates slightly over the elevation lows. Under such conditions the elevation highs exert no control on the flow, and are effectively drowned. In Figure 23c the flow again has the same discharge, and the bed has the same mean slope as Figures 23a and 23b, but the amplitude of the bed undulation is sufficiently high to cause the elevation highs to act as hydraulic controls. This forces Froude-critical flows at the elevation highs, Froude-supercritical flow just downstream of the highs and a hydraulic jump to subcritical flow farther downstream (e.g. Henderson 1966).

One can conceive of a turbidity current analogous to the open channel flow of Figure 23b, i.e. one that is so much thicker than the relief of each minibasin that it flows over the topography as a Froude-subcritical flow, completely drowning the ridges. Such

thick turbidity currents would show little response to the successive ridges and basins of a field of minibasins. They are not the subject of the analysis described here.

**What is the role of flow setup in the morphodynamics of minibasin filling?** Here setup refers to the process by which the head of the turbidity current advances to the downstream end of the barrier, reflects to form an upstream-migrating bore, and stabilizes as an internal hydraulic jump, as described in Figure 19. The role of flow setup in the morphodynamics of minibasin filling is dominant when the duration of the turbidity current is too short to set up quasi-equilibrium ponding. It remains important when the duration of the turbidity current is longer than, but of the same order of magnitude as that necessary to set up quasi-equilibrium ponding. It becomes negligible when the duration is long compared to the setup time for ponding. The last case is the one of primary interest in the present analysis. A setup time of 12.3 minutes was estimated for the prototype basin of Table 4; Lamb et al. (2004) estimate a characteristic setup time for the minibasins on the north slope of the Gulf of Mexico on the order of 30 minutes. Lamb et al. (2004) have studied both surging, or pulse-like turbidity currents that were too short for the setup of quasi-steady ponding as well as fully ponded flows.

**Can a hydraulic jump to ponded flow with no outflow of the turbidity current be expected to be maintained indefinitely?** The condition of no outflow cannot be maintained indefinitely. As succeeding sustained flow events create ponded conditions and force filling of the basin floor, the settling interface should eventually rise above the downstream lip of the barrier. Overflow restricts further rise in the settling interface, so that as the basin floor continues to aggrade the degree of ponding is reduced and an ever weaker hydraulic jump migrates downstream, as described in Figure 24.

**How can the sediment in the ponded zone be held in suspension in the ponded zone where the turbulence is dying?** The sediment is not held in suspension by anything; it is constantly settling out at fall velocity $v_s$. The reason that the suspended sediment concentration remains constant in space and time up to the settling interface is because as sediment settles out on the bed, it is replaced at the same rate from upstream. As long as the flow is sufficiently ponded the settling interface must remain nearly horizontal. Were it to deviate from horizontal, the resulting streamwise pressure forces would create the very weak flow needed to restore it to horizontal. This process is described in Figure 10 of the companion paper, Toniolo et al. (submitted).

In the event, turbulence within a flow field has no capacity to “hold” sediment in suspension. This is best illustrated in the context of the famous experiments of Einstein (1968). In the experiments, steady, uniform highly turbulent flow over an immobile openwork gravel deposit was created in a recirculating flume. Sand was introduced into the flume and allowed to recirculate with the flow, as illustrated in Figure 25a. Were the flow have an intrinsic ability to “hold” the sand in suspension, the flow would have eventually reached an equilibrium state with an equilibrium profile of suspended sediment. Instead the water always eventually clarified completely, as shown in Figure 25b. This is because the sand settled through the layer of openwork gravel and deposited on the bottom of the flume at a depth where it could not be resuspended by the flow.

Complete clarification of the flow occurred not because the flow was not turbulent, but because the flow configuration prevented reentrainment of suspended sediment as it settled out. In the experiments of Einstein (1968), the openwork gravel acted to suppress resuspension, even though the near-bed flow (i.e. the flow near the

surface of the openwork gravel layer) was sufficiently turbulent to resuspend sand were it present there. In the present analysis, the ponded zone of the minibasin may contain antecedent, dying turbulence from the hydraulic jump and the flow upstream. In a sufficiently slow-moving, highly ponded flow, however, the rate of generation of near-bed turbulence can be expected to be too low to resuspend sediment once it settles out.

**How would the process of deposition in a ponded zone proceed when the turbidity current carries multiple grain sizes?** The present analysis assumes a slope break in the initial streamwise profile of the minibasin, a single grain size in suspension and a barrier at the downstream end of the domain. The barrier forces a hydraulic jump to a ponded zone characterized by a single settling interface, and a deposit in the ponded zone that is of uniform thickness in the streamwise direction (Figure 4a of the companion paper, Toniolo et al. submitted). Were the barrier to be removed and the hydraulic jump to be mediated by only the slope break, the deposit would be expected to thin exponentially downstream (Figure 4b of the companion paper, Toniolo et al. submitted).

The case of sediment mixtures has not been considered here. It is nevertheless of value to consider how a flow containing a discrete number of sediment sizes might behave. Multiple grain sizes might be expected to produce multiple settling interfaces, proceeding from lower to higher in the vertical in order of declining grain sizes, as illustrated in Figure 26.

**Should not the deposit in the ponded zone become thinner and finer in the downstream direction?** Again consider Figure 26. The settling interfaces for the coarser material can be expected to intersect the bed at points upstream of the intersection for finer material. As a result the finer material would be expected to overspill the basin first as the bed aggrades. In addition, the bed deposit would be expected to show a pattern of weak downstream thinning and fining. This pattern is precisely that observed by Lamb et al. (submitted) in ponded flows carrying a mixture of sizes in an experimental minibasin. The downstream thinning and fining can be expected to be much weaker than, however, the case of a hydraulic jump at a slope break with no barrier downstream illustrated in Figure 4a of the companion paper, Toniolo et al. (submitted).

**Does the process of flow setup in the ponded basin cause repeated reflection of the turbidity current?** Repeated reflection is precisely what was observed in the case of the surging, or pulse-like turbidity currents flowing into a minibasin studied by Lamb et al. (2004). In the case of the sustained turbidity currents flowing into a minibasin studied by Lamb et al. (2004; submitted) and in the companion paper, Toniolo et al. (submitted), all (case of no overflow) or part (case of overflow) of the front of the tubidity current reflected off the downstream end of the basin, creating an upstream-migrating bore that eventually stabilized upstream. In such a case there is no repeated reflection aside from some occasional minor seiching.

**What would be the effect of lateral expansion in a field minibasin?** The effect of lateral expansion only increases the tendency of a sustained turbidity current to form a highly ponded zone in a minibasin. Violet et al. (in press) have performed experiments on ponding in a minibasin that is much wider than the zone of inflow to it.

**Why does the turbidity current not drop out its sediment before it reaches a downstream barrier such as the downstream end of a minibasin with no outlet?** Consider the geometry of Figure 1. It is possible that the turbidity current might deposit its sediment beyond the slope break, with or without a hydraulic jump, before reaching

the downstream barrier. In such a case the downstream barrier plays no role whatsoever in the deposit. The present analysis applies only to turbidity currents that are sufficiently powerful to reach the downstream end of the minibasin, and sufficiently sustained to allow the setup of quasi-steady ponded flow.

**Does the formulation address the possibility of deposits of massive sands?** One kind of turbidite consists of a massive sand. Such deposits show little or no structure such as ripples or laminations indicating that the suspended sediment passed through a bedload layer as it settled out. In addition, massive sands often show little change in characteristic grain size in the vertical. It has been speculated that massive sands are emplaced by "high-density turbidity currents" (e.g. Kneller and Branney 1995).

The present analysis is not specifically designed to explain the emplacement of massive sands. It does, however, offer an alternative emplacement mechanism in terms of the ponding of a sustained, sand-rich, turbidity current. If the degree of ponding is sufficient, the sand will not be resuspended, or even reworked by bedload as it settles out. Now consider the case of sustained flow that is constant in time. For the sake of argument it is assumed that a minibasin captures all of the incoming turbidity current. The grain size distribution of the material that is deposited must thus remain constant in time, and equal to the grain size distribution of the material (constantly) arriving from upstream. A deposit created by such a flow would not display any upward fining. (It could be expected, however, to be capped by a deposit showing upward fining as the sustained flow finally wanes.) The upscaling of Experiment 1 in Table 3 suggests that ponding of dilute, sand-rich turbidity currents offers a viable alternative to "high-density turbidity currents" for the formation of massive sands.

Leclair and Arnott (2003) have performed experiments illustrating the suppression (but not elimination) of laminations in sandy deposits downstream of a hydraulic jump of a turbidity current induced by a barrier. The volume concentration of sand in their turbidity currents was sufficiently high to render the flows non-dilute.

**How could the ponding described in this paper lead to the relatively uniform long profiles of channels through many minibasins, with canyons excavated across the ridges and filling in the minibasins, as observed the East Breaks basins?** The East Breaks minibasins were introduced in the companion paper, Toniolo et al. (submitted); the channel long profile across four minibasins separated by three ridges is given in Figure 2b therein (Beaubouef and Friedman 2000). The analysis given here pertains to the first stages of spillover to the minibasin of interest from the minibasin just updip. Initially the inflow may be fine-grained, and the minibasin may capture all flow events, including sustained events, because the settling interface does not rise to the height of the basin lip at the downstream end. As the minibasin updip fills, the overflow into the basin of interest should become stronger and include coarser material. As a result the overflow may become competent to gradually excavate a canyon into the ridge. As sedimentation proceeds in the basin of interest, the settling interface should eventually rise above the lip, and overflow of turbidity currents containing finer grains should commence. The ultimate evolution of the long profile thus likely includes both filling of the basins and scour into the ridges just updip. The model presented here thus addresses an essential part, but nevertheless only a part of the evolution of the long profile of a channel connecting many minibasins.

The model presented here is thus intended to be the first step toward a model that is able to encompass a) multiple grain sizes, b) 3D minibasin topography and c) erosion as well as deposition, so being able to capture the morphodynamics of the evolution of the long profile shown in Figures 2b and 2c of the companion paper, Toniolo et al. (submitted), and the resulting deposit stratigraphy.

## INTERNAL DELTAS: A SPECULATION

A lake can be viewed as a ponded river created by a basin with a downstream barrier, in the same way that minibasins can pond turbidity currents. As a river flows into a lake, it decelerates to form a delta with a coarse-grained (and often channelized) topset, a coarse-grained foreset, and a fine-grained bottomset. If the river flow is not too heavily charged with fine-grained material, the bottomset is formed from passive rain from a muddy plume beyond the foreset (Figure 27a).

The nature of the deposit at the end of Experiment 1 in Figure 6a looks remarkably like a foreset immediately followed by a bottomset. Beaubouef et al. (2003) report that Basin IV of the East Breaks minibasins (Figure 2 of the companion paper, Toniolo et al., submitted) appears to have a coarse-grained, channelized, prograding topset, a low foreset and a fine-grained bottomset with a draped deposit (Figures 2 and 3 therein). The structure of the bottomset suggests that it was emplaced by a ponded turbidity current. It is speculated here that under the right circumstances the process of ponding can lead to the formation of an internal delta in a deep-sea minibasin that has some similarities to fluvial deltas. The speculation is illustrated in Figure 27b.

## CONCLUSIONS

The physically-based theory of sedimentation in minibasins presented in the companion paper, Toniolo et al. (submitted) identifies a heretofore poorly-recognized flow regime, i.e. a ponded turbidity current. The ponding is created by an elevation barrier. It forces a relatively swift, Froude-supercritical turbidity current to pass through a type of shock known as an internal hydraulic jump, which results in a deep, placid, slow-moving turbidity current farther downstream. This ponded current may a) be incapable of eroding bed sediment into suspension and b) have virtually no turbulent mixing at the settling interface between the ponded turbid water and the clear water above. In the case of uniform sediment, this results in a) a deposit consisting of a drape of near-uniform thickness and b) active upward detrainment of clear water across a distinct, glassy settling interface. The loss of both sediment and water from the current due to settling and detrainment can weaken it to the point that no overflow whatever occurs, even with continuous inflow.

In the present paper this model of minibasin flow and deposition mechanics has been implemented numerically and checked against experiments for a slot-like minibasin and a turbidity current with a single grain size. Several predictions of the theory have been verified, including the nearly uniform thickness of the deposit in the ponded zone and the existence of conditions for which overflow of neither water nor sediment occurs at the downstream lip of the basin. Calculations at field scale yield detrainment discharges ranging from thousands to hundreds of thousands of cubic meters per second, indicating that ponding and associated detrainment can act as a strong control on the

process of minibasin "fill and spill." More precisely, they indicate that significant spill to the next basin downdip may not be realized until the basin in question is filled with sediment to the point that ponding is insufficient to capture the full flow.

The present model is somewhat limited in its applicability to the field due to the restrictions of a single grain size, a slot-like geometry, a near-vertical wall at the downstream end of the minibasin and the exclusion of bed erosion. Further progress will require the relaxation of these constraints.

## ACKNOWLEDGMENTS

This research was supported by the Office of Naval Research STRATAFORM Program and the St. Anthony Falls Oil Consortium and ExxonMobil Upstream Research Co.

## REFERENCES

BADDOUR, R. E., 1987, Hydraulics of shallow and stratified mixing channel: *Journal of Hydraulic Engineering*, 113(5), 630-645.

BAGNOLD, R. A., 1966, An approach to the sediment transport problem from general physics: US Geol. Survey Prof. Paper 422-I, Washington, D.C.

BEAUBOUEF, R.T., AND FRIEDMAN, S.J., 2000, High resolution seismic/sequence stratigraphic framework for the evolution of Pleistocene intra slope basins, western Gulf of Mexico: depositional models and reservoir analogs: *GCSSEPM Foundation 20th Annual Research Conference*, Deep-Water Reservoirs of the World, Dec. 3-6, 40-60.

BEAUBOUEF, R.T, VAN WAGONER, J.C. AND ADAIR, N.L., 2003, Ultra-high resolution 3-D characterization of deep-water deposits- II: Insights into the evolution of a submarine fan and comparisons with river deltas: *Extended Abstract*, Annual Convention, American Association of Petroleum Geologists, Salt Lake City, Utah, May 11 – 14, 9 p.

DIETRICH, E.W., 1982, Settling velocities of natural particles: *Water Resources Research*, 18 (6), p. 1626 – 1682.

EINSTEIN, H. A., 1968, Deposition of suspended particles in a gravel bed: *Journal of Hydraulic Engineering*, 91(4), 225-247.

ETTEMA, R., ARNDT, R., ROBERTS, P. AND WAHL. T, 2000, Hydraulic Modeling: Concepts and Practice: *No.* 97, Manuals and Reports on Engineering Practice, American Society of Civil Engineers, 390 p.

FUKUSHIMA, Y, PARKER, G. AND PANTIN, H. M., 1985, Prediction of ignitive turbidity currents in Scripps Submarine Canyon: *Marine Geology*, 67, 55-81.

GARCIA, M.H., 1993, Hydraulic jumps in sediment-driven bottom currents: *Journal of Hydraulic Engineerin*g, ASCE, 119(10), 1-24.

GARCIA, M.H., AND PARKER, G., 1989, Experiments on hydraulic jumps in turbidity currents near a canyon-fan transition: *Science*, 245, 393-396.

GARCIA, M. AND PARKER, G., 1993, Experiments on the entrainment of the sediment into suspension by a dense bottom current: *Journal of Geophysical Research*, 98, 4793-4807.

GHARANGIK, A.M. AND CHAUDRY, M.H., 1991, Numerical simulation of hydraulic Jump: *Journal of Hydraulic Engineerin*g, ASCE, 117(9), 1195-1211.

HICKSON, T., SHEETS, B., AND MARR J., 2000, Filling of intraslope basins by turbidity currents: results from experimental simulations: *Abstracts*, American Association of Petroleum Geologists, 2000 Annual Convention, April 16-19.

JAMESON, A., SCHMIDT W., AND TURKEL, E., 1981, Numerical solutions fo the Euler equations by finite volume methods using Runge-Kutta time-stepping schemes: *AIAA 14th Fluid and Plasma Dynamics Conf.: AIAA 81 –1259.* American Institute of Aeronautics, Palo Alto, Calif.

KNELLER, B. AND BRANNEY, M.J., 1995, Sustained high-density turbidity currents and the deposition of thick massive sands: *Sedimentology*, 42, 607-616.

LAMB, M. P., TONIOLO, H. AND PARKER, G, 2001, Deposition by turbidity currents in intraslope diapiric minibasins: results of 1-D experiments and numerical modeling. *Eos Trans. AGU*, 82(47).

LAMB, M.P., HICKSON, T., MARR, J.G., SHEETS, B., PAOLA, C. AND PARKER, G.,. 2004, Surging versus continuous turbidity currents: flow dynamics and deposits in an experimental intraslope minibasin:*Journal of Sedimentary Research,* 74(1), pp. 148-155.

LAMB, M. P., TONIOLO, H. AND PARKER, G, in review, Trapping of continuous turbidity currents by intraslope minibasins: *Sedimentology*, downloadable at: http://www.ce.umn.edu/~parker/preprints.htm .

LECLAIR, S. AND ARNOTT, W., 2003, Coarse-tail graded, structureless strata: Indicators of an internal hydraulic jump: *Shelf Margin Deltas and Linked Down Slope Petroleum Systems: Global Significance and Future Exploration Potential.* 23rd Annual GCS-SEPM Foundation Bob F. Perkins Research Conference, H. Roberts, N. Rosen, R. Filion, and J. Anderson, Eds., 817-835.

MACCORMACK, R., 1969, The effect of viscosity in hypervelocity impact cratering: *Paper* 69-354, American Institute of Aeronautics and Astronautics, Cincinnati, Ohio.

PARKER, G., 1991, Selective sorting and abrasion of river gravel. II: Applications: *Journal of Hydraulic Engineering*, 117(2): 150-171.

PARKER, G., FUKUSHIMA, Y., AND PANTIN, H.M., 1986, Self-accelerating turbidity currents: *Journal of Fluid Mechanics* 171, pp. 145-181.

STEFAN, H. AND HAYAKAWA, N., 1972, Mixing induced by an internal hydraulic jump: *Water Resources Bulletin*, 8 (3), 531-545.

TANNEHILL, J., ANDERSON, D., AND PLETCHER, R., 1997, Computational Fluid Mechanics and Heat Transfer, second edition: Taylor & Francis, Washington DC, 792 p.

TONIOLO, H., LAMB. M., AND PARKER, G., submitted, Depositional turbidity currents in diapiric minibasins on the continental slope: formulation and theory: *Journal of Sedimentary Research*.

VIOLET, J., EVANS, C., SHEETS, B., PAOLA, C., PRATSON, L. AND PARKER, G., 2001, Filling of a salt-withdrawal minibasin on the continental slope by turbidity currents: Experimental Study: *Eos Trans. AGU*, 82(47).

VIOLET, J., SHEETS, B., PRATSON, L., PAOLA, C., BEAUBOUEF, R. T. AND PARKER, G., accepted, Experiment on turbidity currents and their deposits in a model 3D subsiding minibasin: *Journal of Sedimentary Research*, downloadable at http://www.ce.umn.edu/~parker/preprints.htm.

WILKINSON, D. L. AND WOOD, I. R., 1971, A rapidly varied flow phenomenon in a two-layer flow: *Journal of Fluid Mechanics*, 47 (2), 241-256.

WRIGHT, S. AND PARKER, G., 2004, Flow resistance and suspended load in sand-bed rivers: simplified stratification model: *Journal of Hydraulic Engineering*, 130(8), 796-805.

## NOTATIONS

| | |
|---|---|
| $A, B$ | vectors defined by Equations 11 and 12 |
| $A_i^*, A_i^{**}$ | predictor and corrector forms for the vector $A$, as defined by Equations 14 and 15, respectively |
| $B_b$ | width of the basin |
| $C$ | layer-averaged volume concentration in the turbidity current |
| $C_{aj}$ | layer-averaged volume concentration in the turbidity current just after the hydraulic jump |
| $C_{bj}$ | layer-averaged volume concentration in the turbidity current just before the hydraulic jump |
| $C_{fl}$ | interfacial friction coefficient |
| $C_{fo}$ | bed friction coefficient |
| $C_{foaj}$ | bed friction coefficient just after the hydraulic jump |
| $C_{fobj}$ | bed friction coefficient just before the hydraulic jump |
| $C_n$ | Courant number |
| $C_u$ | layer-averaged volume concentration in the turbidity current at the upstream end of the basin |
| $c'$ | concentration in scale relations |
| $D_g$ | mean size of the glass beads used in the experiments |
| $D_s$ | characteristic grain size |
| $D_{50}$ | median size of the glass beads used in the experiments |
| $E_s$ | dimensionless coefficient of entrainment of bed sediment into suspension |
| $e_w$ | dimensionless coefficient of water entrainment |
| $\boldsymbol{Fr_d}$ | densimetric Froude number |
| $g$ | acceleration of gravity |
| $h$ | turbidity current thickness |
| $h_{aj}$ | turbidity current thickness just after the hydraulic jump |
| $h_{bj}$ | turbidity current thickness just before the hydraulic jump |
| $h_u$ | turbidity current thickness at the upstream end of the basin |
| $i$ | index for spatial discretization |
| $k$ | index for time discretization |
| $k_s$ | bed roughness height |
| $L_b$ | length of the basin |
| $L_p$ | length of the ponded zone of the turbidity current |
| $\ell'$ | length in scale relations |
| $Q$ | flow discharge of the turbidity current |
| $Q_{aj}$ | flow discharge of the turbidity current just after the hydraulic jump |
| $Q_{bj}$ | flow discharge of the turbidity current just before the hydraulic jump |
| $Q_d$ | detrainment discharge of a ponded turbidity current |
| $Q_u$ | flow discharge of the turbidity current at the upstream end of the basin |

| | |
|---|---|
| $Q'$ | discharge in scale relations |
| $Q_1$ | inflow discharge in field scale simulation |
| $R$ | $= (\rho_s/\rho - 1)$, submerged specific gravity of sediment |
| $\boldsymbol{Ri}$ | bulk Richardson number defined by Equation 6b |
| $r_o$ | coefficient relating near-bed volume suspended sediment concentration $c_b$ to the layer-averaged value $C$, such that $c_b = r_o C$ |
| $S$ | bed slope |
| $S_{b1}$, $S_{b2}$ | bottom slopes of the experimental minibasin |
| $t$ | time |
| $T_s$ | setup time |
| $t'$ | time in scale relations |
| $U$ | layer-averaged streamwise velocity |
| $U_{aj}$ | layer-averaged streamwise velocity just after the hydraulic jump |
| $U_{bj}$ | layer-averaged streamwise velocity just before the hydraulic jump |
| $U_u$ | layer-averaged streamwise velocity at the upstream end of the basin |
| $u'$ | velocity in scale relations |
| $u_*$ | shear velocity |
| $v_s$ | fall velocity of the sediment in the turbidity current |
| $x$ | streamwise direction |
| $Z$ | vector defined by Equation 13 |
| $\Delta h_b$ | maximum relief |
| $\Delta h_{bo}$ | height of the bore |
| $\Delta x$, $\Delta t$ | spatial and time steps in the numerical discretization |
| $\delta$ | parameter in Equations 9a and 9c equal to unity in the ponded zone and zero in the supercritical zone upstream of the submerged hydraulic jump |
| $\varepsilon_i$ | damping parameter defined in Equation 17 |
| $\kappa$ | damping parameter defined in Equation 18 |
| $\lambda$ | scale ratio |
| $\lambda_M$ | $= \Delta t/\Delta x$ |
| $\lambda_p$ | sediment porosity |
| $\eta$ | bed elevation |
| $\eta_I$ | antecedent bed elevation |
| $\xi$ | interface elevation |
| $\xi_o$ | water surface elevation |
| $\rho$ | density of water |
| $\rho_s$ | density of sediment |
| $\tau_b$ | bed shear stress |
| $\theta_{b1}$, $\theta_{b2}$ | bed slope angles in the experimental minibasin |
| $\sigma_g$ | geometric standard deviation of the glass beads used in the experiments |
| $(\ )_m$ | any value in the model |
| $(\ )_p$ | any value in the prototype |

## FIGURE CAPTIONS

**Figure 1** Sketch of a supercritical turbidity current flowing into into a deep basin, showing the hydraulic jump, the ponded zone and overflow (or the lack thereof) at the downstream lip.

**Figure 2** Sketch of the facility where the experiments were performed.

**Figure 3** Sketch of the experimental minibasin built into the flume.

**Figure 4** Grain size distribution of glass beads used in the experiments.

**Figure 5** Picture showing horizontal settling interface during Experiment 1. The flow was on when the picture was taken.

**Figure 6** a) Photographs illustrating the final deposit of Experiment 1. Coal and color marks on the wall were used to identify the bed position at different times during the experiment. The flow was from left to right. The deposit thickness is very uniform in the ponded zone. Numbers in the photographs indicate the distance in inches from the upstream end of basin.

b) Picture showing the sediment-free bed downstream of the barrier at the end of Experiment 1. The white material at the bottom downstream end of the barrier is adhesive, not sediment.

**Figure 7** View of the final deposit of Experiment 3. Sediment is seen to be deposited both within and beyond the downstream lip of the basin due to high flow discharge of the experiment. The flow was from left to right.

**Figure 8** Bed elevations at different times for Experiment 1; also illustrated are the positions of the siphon rakes, as well as the elevation of the interface between turbid and clear water.

**Figure 9** Bed elevations at different times for Experiment 3; also illustrated are the positions of the siphon rakes, as well as the elevation of the interface between turbid and clear water.

**Figure 10** Diagrams illustrating the vertical profiles of suspended sediment concentration at various times for Experiment 1. The water surface during the experiment was 60 cm above the initial bed. The interface elevation refers to the profiles in the ponded zone, i.e. excluding the profile farthest upstream.

a) Run time: 16 minutes
b) Run time: 38 minutes
c) Run time: 58 minutes

**Figure 11** Diagram illustrating the vertical profiles of suspended sediment concentration for Experiment 3 at a run time of 8 minutes. The water surface during the experiment was 60 cm above the initial bed. The interface elevation refers to the profiles in the ponded zone, i.e. excluding the profile farthest upstream.

**Figure 12** Vertical profiles of the geometric mean size of the suspended sediment in Experiment 1 at a run time of 58 minutes.

**Figure 13** Vertical profiles of the geometric mean size of the suspended sediment in Experiment 3 at a run time of 8 minutes.

**Figure 14** Long profile of grain size associated with the peaks of the probability density profiles of grain size distribution for the samples of bed material collected at the end of Experiment 1.

**Figure 15** Long profile of grain size associated with the peaks of the probability density profiles of grain size distribution for the samples of bed material collected at the end of Experiment 3.

**Figure 16** Photograph showing the downstream end of the minibasin during Experiment 1. The interface between muddy and clear water is located below the downstream overflow lip. The flow direction is from right to left. The flow was on when the picture was taken.

**Figure 17** Photograph showing the downstream end of the minibasin during Experiment 3. The interface between muddy and clear water is located above the downstream overflow lip. The flow direction is from right to left. The flow was on when the picture was taken.

**Figure 18** Diagram illustrating comparison between the bed profile measured during Experiment 1 and the prediction of the numerical model. The run time is 16 minutes.

**Figure 19** Diagram illustrating the setup of ponded flow in Experiment 1 as predicted by the numerical model, including a) propagation of the front of the turbidity current, b) runup of the front against the downstream barrier and c) reflection of the flow as an upstream-migrating bore.

**Figure 20** Diagram illustrating comparison between the bed profile measured during Experiment 3 and the prediction of the numerical model. The run time is 11 minutes.

**Figure 21** Diagram illustrating the variation of a) elevation of the settling interface $\xi$, at a point located 3 m downstream the inlet, b) streamwise flow discharge $Q$, c) layer-averaged volume suspended sediment concentration $C$ in

Experiment 1 predicted by the numerical model. The run time is 16 minutes. The patterns are in accordance with the simplified theoretical model of the companion paper, Toniolo et al. (submitted).

**Figure 22** a) Evolution of the bed in the field-scale minibasin as predicted by the numerical model.
b) Evolution of the interface between turbid and clear water in the field-scale minibasin as predicted by the numerical model.
c) Predicted long profile of flow discharge in the field-scale minibasin at the end of the numerical experiment. The spike at the hydraulic jump is an artifice and should be ignored.
d) Long profile of volume suspended sediment discharge in the field-scale minibasin at the end of the numerical experiment. The spike at the hydraulic jump is an artifice and should be ignored.

**Figure 23** a) Steady, uniform Froude-subcritical open channel flow over a plane bed with constant bed slope.
b) The same water discharge flows over a bed of the same mean bed slope but with a periodic streamwise undulation of relatively small amplitude. The flow remains subcritical everywhere, modestly accelerating over the highs and decelerating over the lows. The highs do not exert hydraulic control on the flow.
c) The same discharge flows over a bed with the same mean bed slope, but with a periodic bed undulation of sufficient amplitude to causes the elevation highs to act as controls on the flow. Froude-critical flow is attained at the highs, and Froude-supercritical flow followed by a jump to Froude-subcritical flow is realized downstream.

**Figure 24** Diagram illustrating the weakening and downstream migration of the hydraulic jump as basin sedimentation proceeds.

**Figure 25** a) Sand is introduced into a highly turbulent flow over a thick layer of immobile, openwork gravel.
b) The water has completely clarified as the sand has settled through the pores of the openwork gravel to the bottom of the flume, where it cannot be resuspended. Adapted from Einstein (1968).

**Figure 26** Sketch of hypothetical depositional patterns in a ponded turbidity current containing multiple grain sizes.

**Figure 27** a) Illustration of a fluvial delta in a lake with a coarse-grained channelized topset emplaced fluvially, a prograding foreset emplaced by avalanching of coarse-grained material

and a fine-grained bottomset emplaced by passive rain from a muddy plume.
b) Speculative illustration of a possible configuration of an internal delta in a minibasin with a coarse-grained, channelized topset, a low, prograding coarse-grained foreset and a fine-grained bottomset emplaced by a ponded turbidity current.

**Table1: Main characteristics of experiments**

| Exp. | Upstr. disch. $Q_u$ (liters/s) | Upstr. flow thickness $h_u$ (cm) | Upstr. conc. $C_u$ | Sed. fall vel. $v_s$ (cm/s) | Duration (minutes) | Sampling time (minutes) (*) | Bed marking Time (minutes) (*) |
|---|---|---|---|---|---|---|---|
| 1 | 0.33 | 1 | 0.05 | 0.14 | 58 | 16, 38, 58 | 16, 38, 58, final deposit |
| 3 | 1.90 | 2 | 0.05 | 0.17 | 11 | 8 | final deposit |

(*) from the beginning of the experiment

**Table 2: Predicted characteristics of the flow**

| Exp. | $Q_{bj}$ lit/s | $U_{bj}$ cm/s | $h_{bj}$ cm | $C_{bj}$ | $\boldsymbol{Fr}_{dbj}$ | $U_{bj}/v_s$ | $Q_{aj}$ lit/s | $U_{aj}$ cm/s | $h_{aj}$ cm | $C_{aj}$ | $\boldsymbol{Fr}_{daj}$ | $U_{aj}/v_s$ | $L_p$ m | $Q_d$ lit/s |
|---|---|---|---|---|---|---|---|---|---|---|---|---|---|---|
| 1 | 1.28 | 22.1 | 1.9 | 0.011 | 4.02 | 158 | 1.28 | 1.1 | 40 | 0.011 | 0.042 | 7.5 | 3.05 | 1.30 |
| 3 | 3.44 | 45.2 | 2.5 | 0.032 | 4.13 | 266 | 3.44 | 2.4 | 48 | 0.032 | 0.049 | 14 | 3.22 | 1.67 |

**Table 3: Results of upscaling of measured parameters of Experiment 1 with a scale ratio $\lambda$ of 1000**

| | $R$ | $v_s$ cm/s | $D_s$ μm | $L_b$ m | $\Delta h_b$ m | $B_b$ m | $Q_u$ $m^3/s$ | $U_u$ m/s | $h_u$ m | $C_u$ | $T_r$ hr | $\boldsymbol{Fr}_{du}$ |
|---|---|---|---|---|---|---|---|---|---|---|---|---|
| model | 1.5 | 0.14 | 42 | 4.06 | 0.46 | 0.304 | 0.00033 | 0.11 | 0.01 | 0.05 | 0.97 | 1.32 |
| prototype | 1.65 | 4.64 | 342 | 4060 | 460 | 304 | 10,900 | 3.59 | 10 | 0.05 | 29.1 | 1.32 |

**Table 4: Results of upscaling of parameters pertaining to the ponded zone of Experiment 1 predicted with the numerical model with a scale ratio $\lambda$ of 1000.**

| | $L_p$ m | $Q_{aj}$ $m^3/s$ | $U_{aj}$ m/s | $h_{aj}$ m | $C_{aj}$ | $Q_d$ $m^3/s$ | $\boldsymbol{Fr}_{daj}$ | $U_{aj}/v_s$ |
|---|---|---|---|---|---|---|---|---|
| model | 3.05 | 0.00128 | 0.011 | 0.400 | 0.011 | 0.00130 | 0.042 | 7.5 |
| prototype | 3050 | 42,500 | 0.35 | 400 | 0.011 | 43,200 | 0.042 | 7.5 |

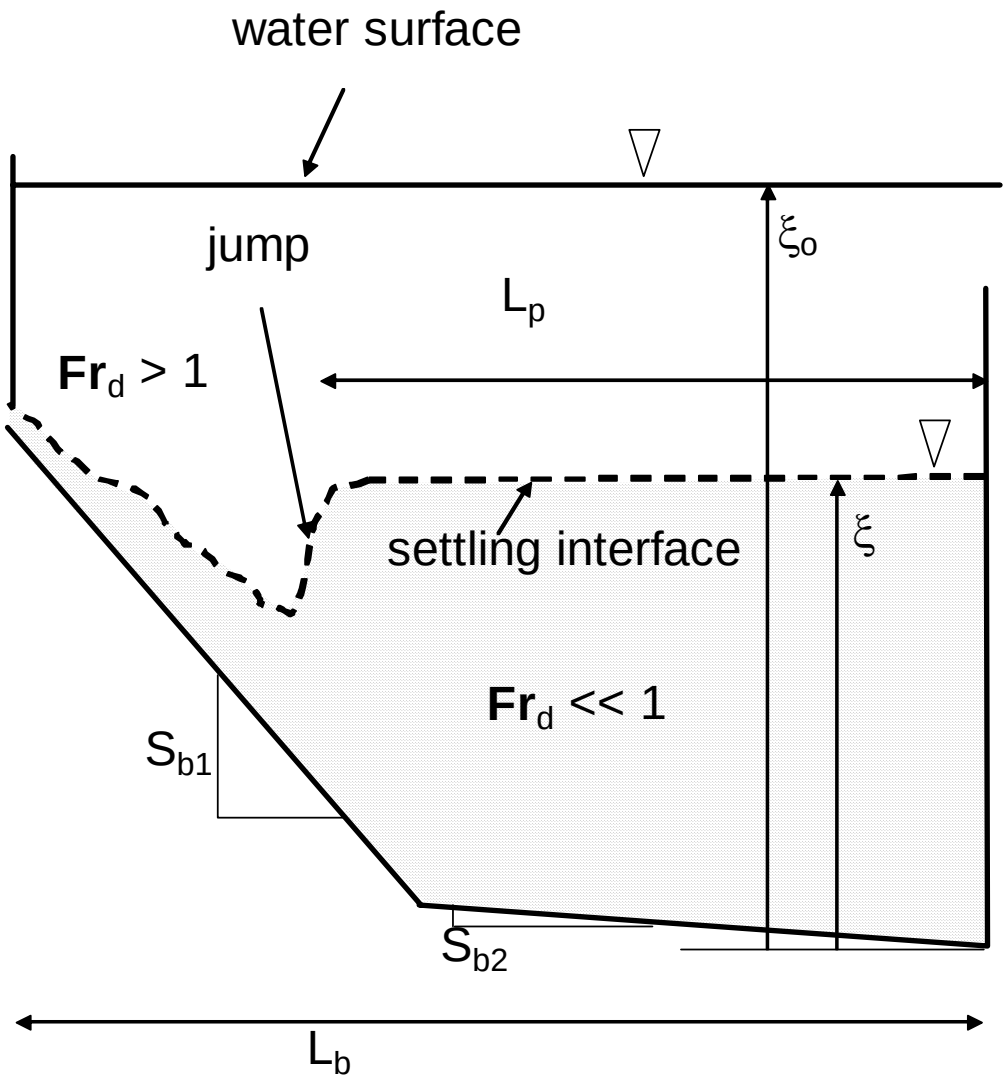
water surface
jump
$\xi_o$
$L_p$
$Fr_d > 1$
settling interface
$\xi$
$Fr_d << 1$
$S_{b1}$
$S_{b2}$
$L_b$

**Figure 1.**

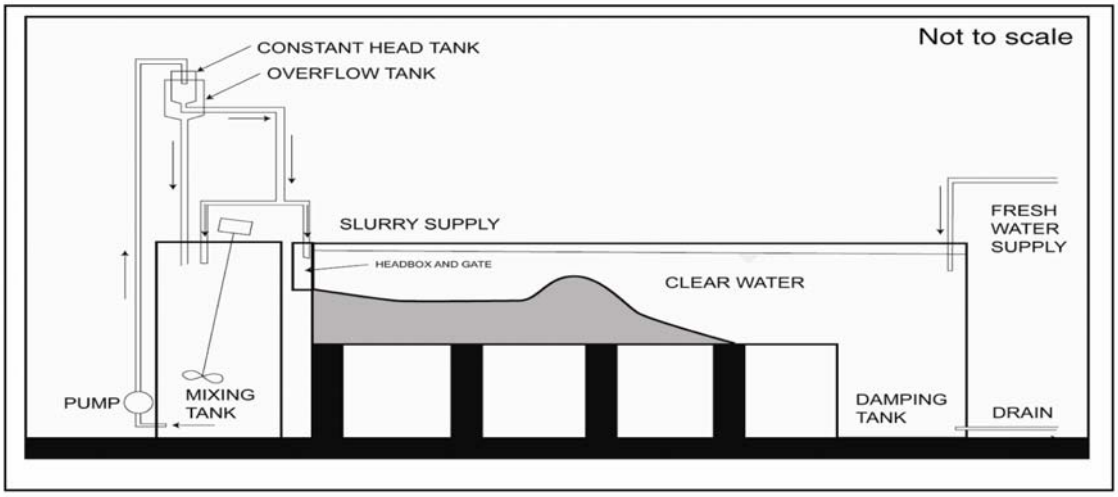


**Figure 2.**

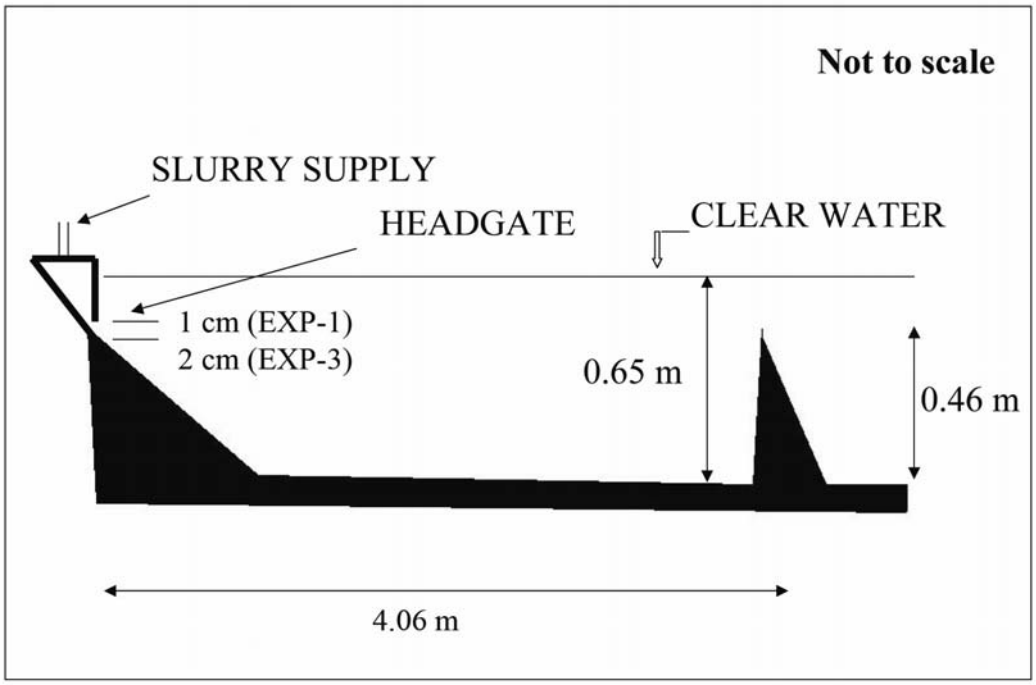


**Figure 3.**

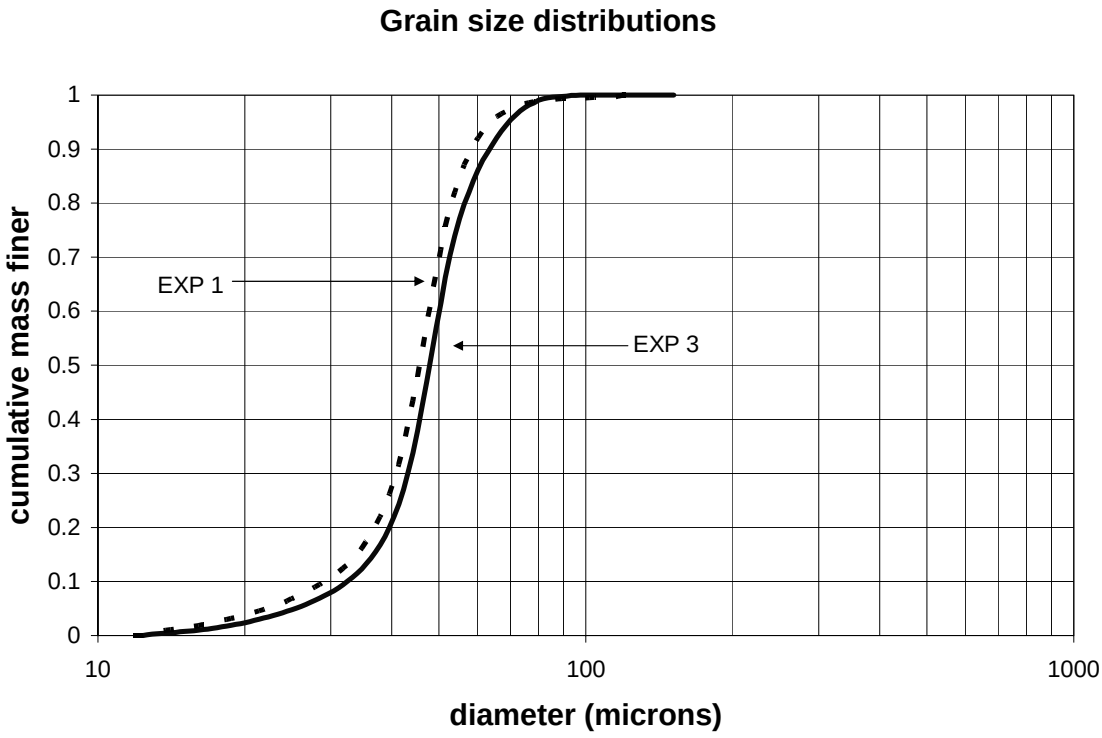


**Figure 4.**

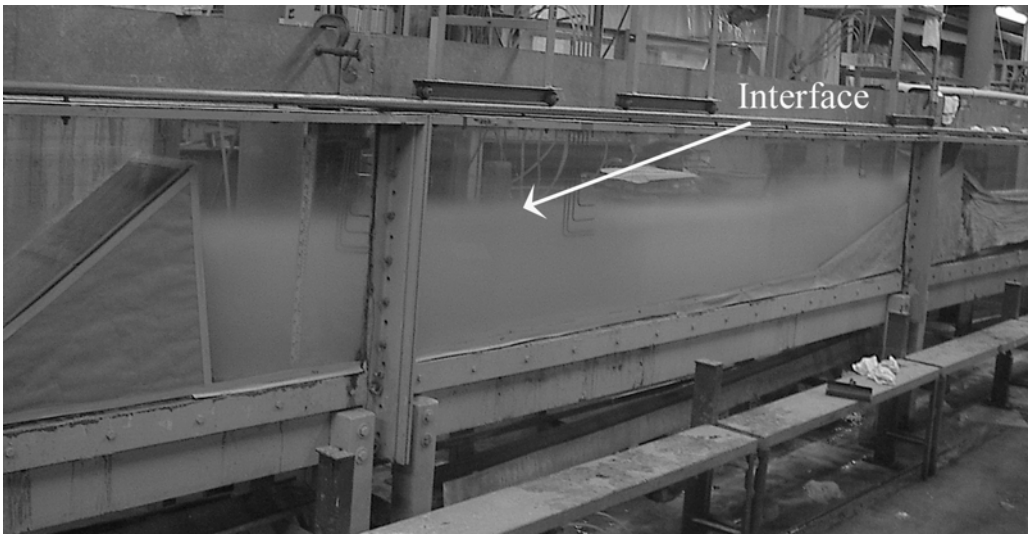


**Figure 5.**

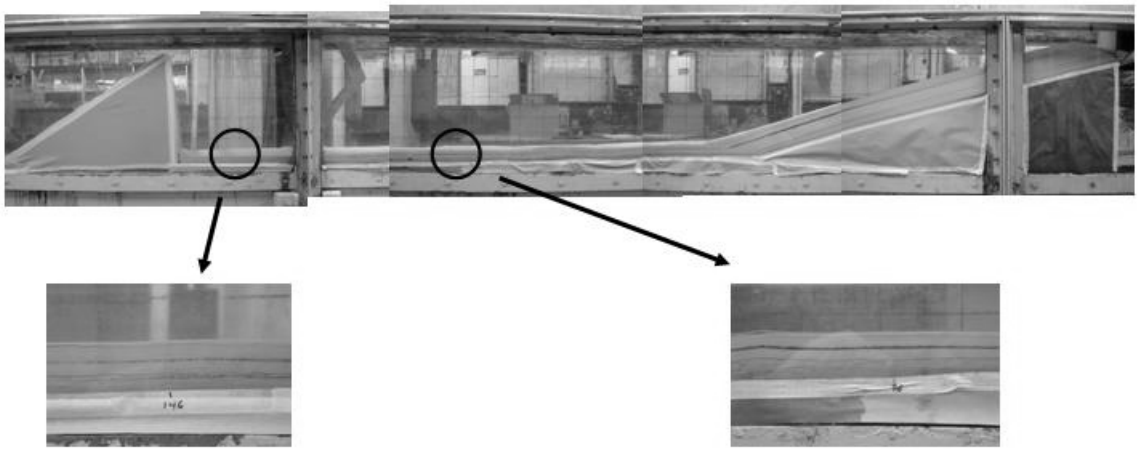

**Figure 6 a**

**Figure 6b**

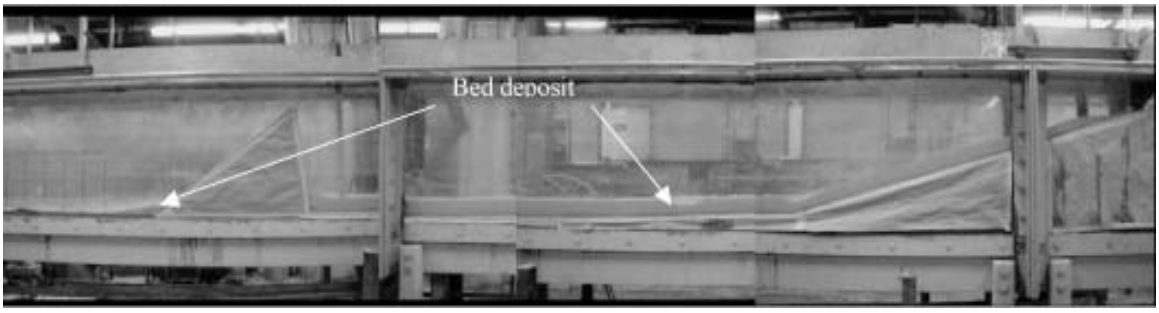


**Figure 7.**

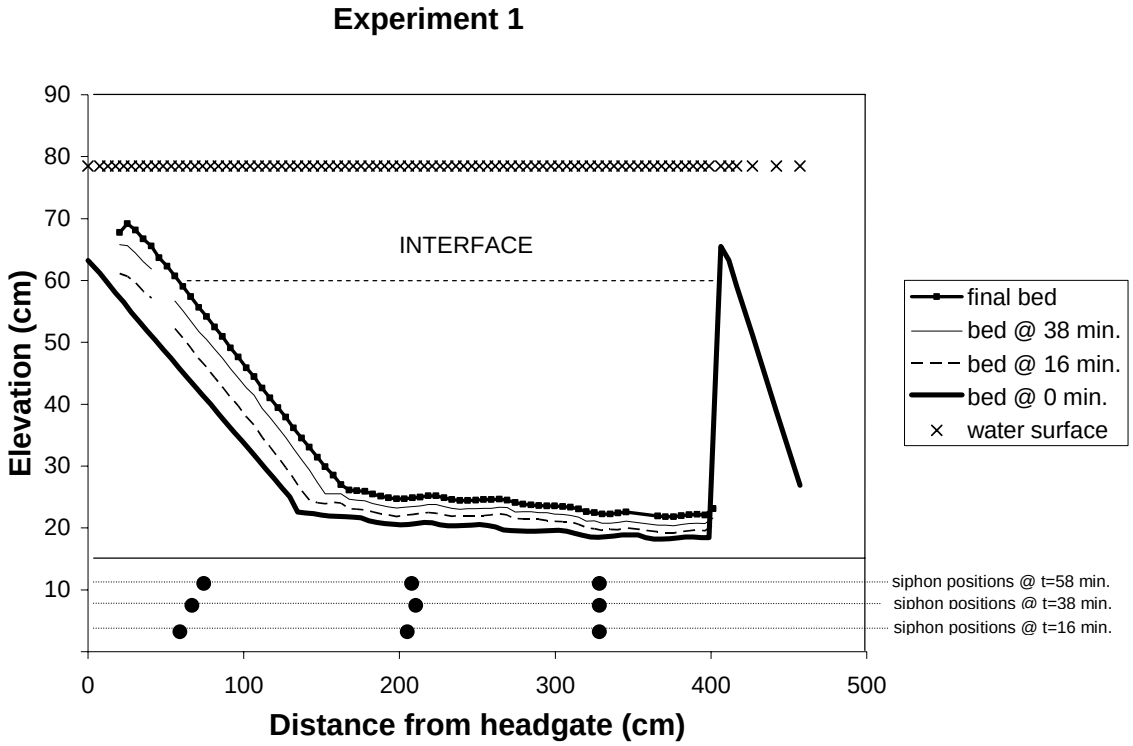


**Figure 8.**

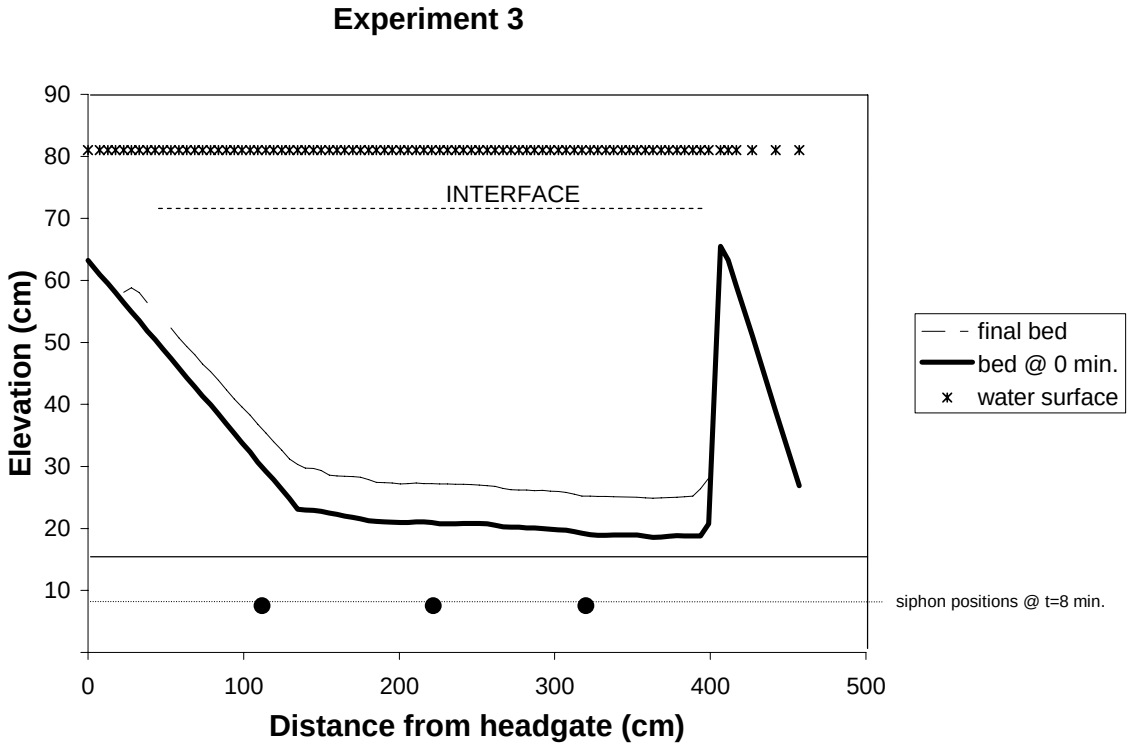


**Figure 9.**

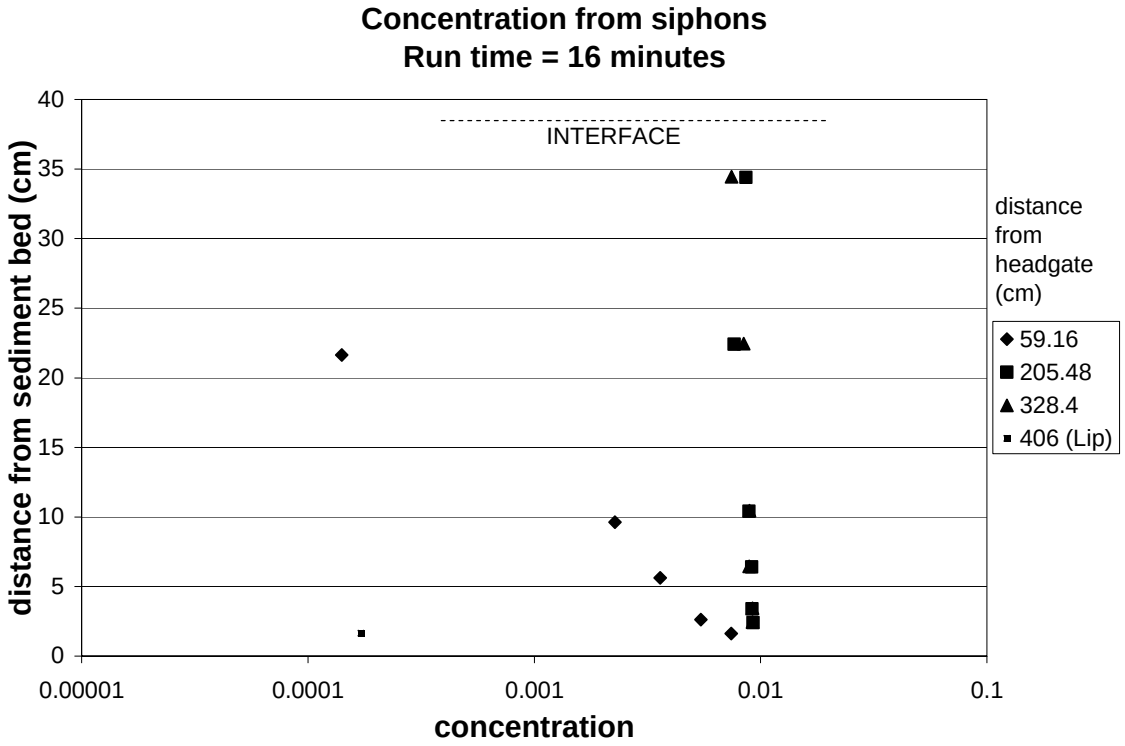


**Figure 10 a**

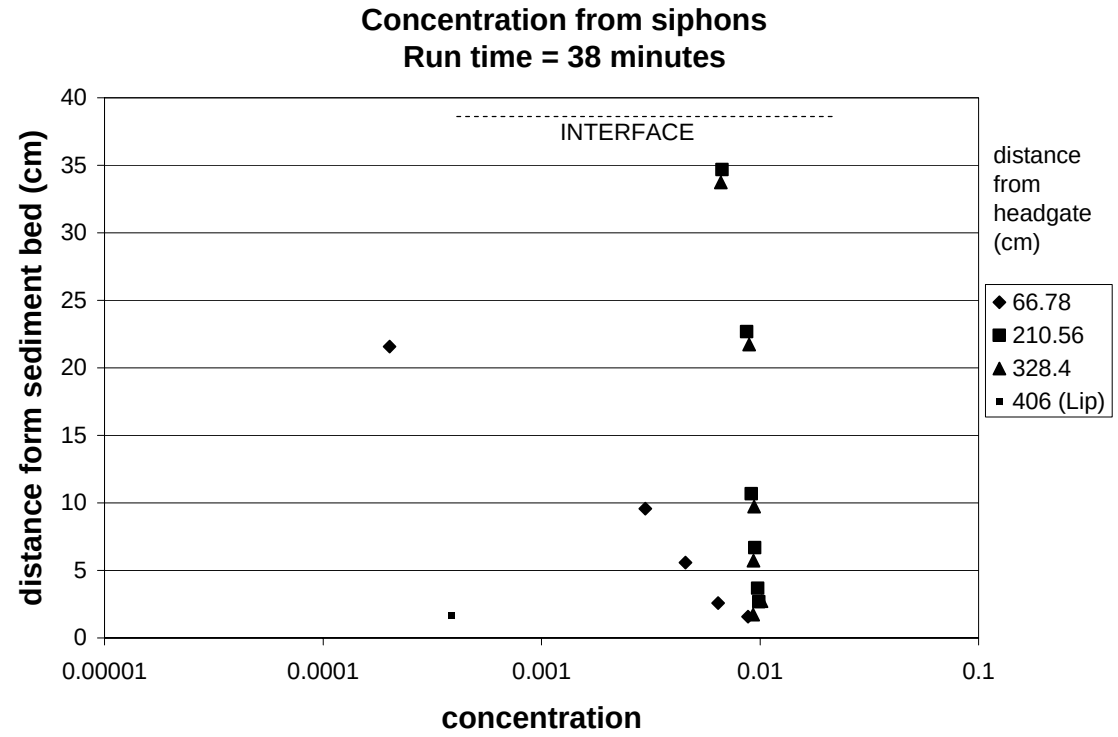


**Figure 10 b**

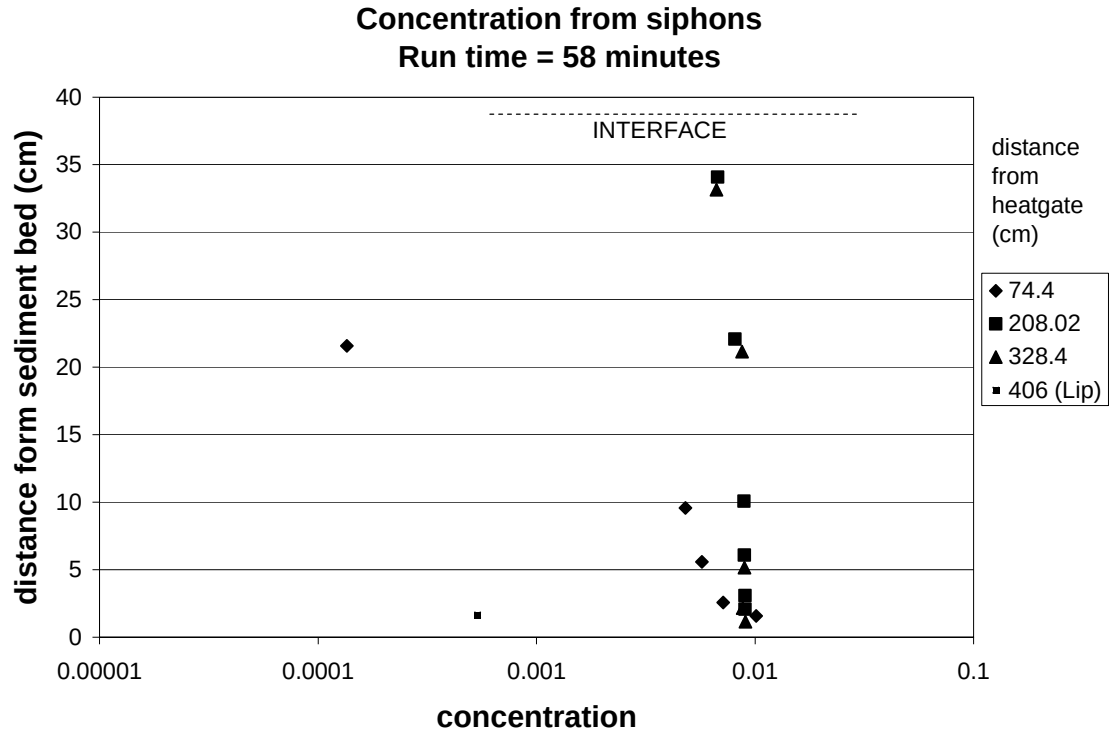


**Figure 10 c**

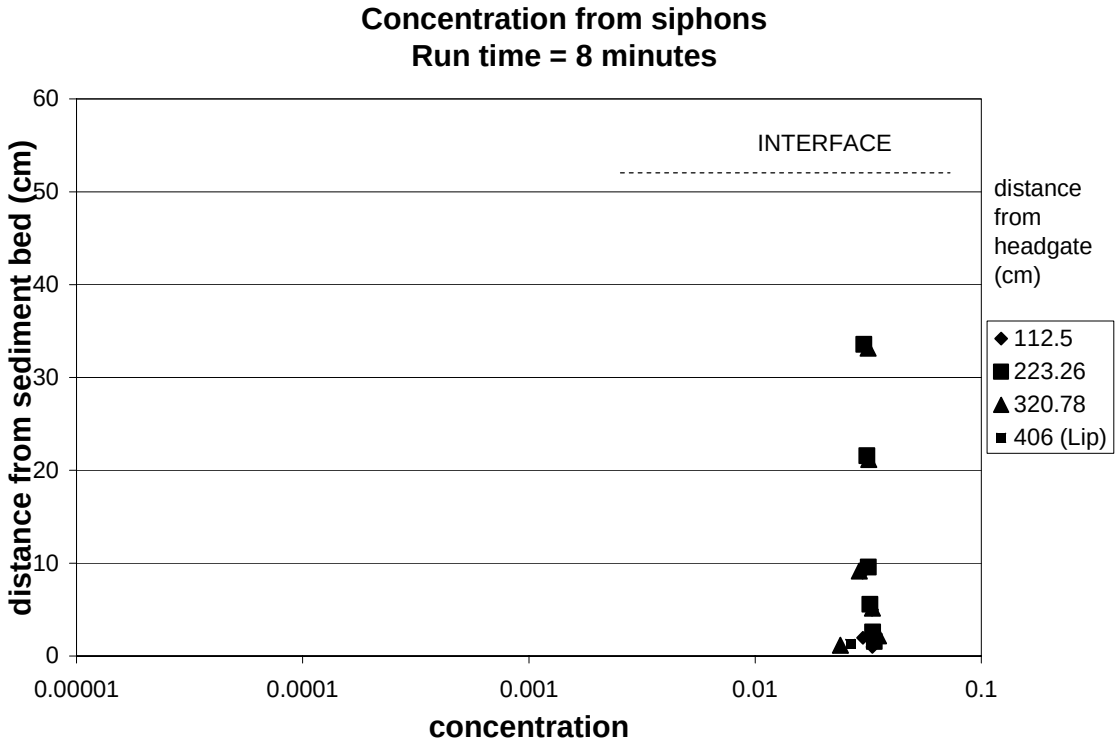


**Figure 11.**

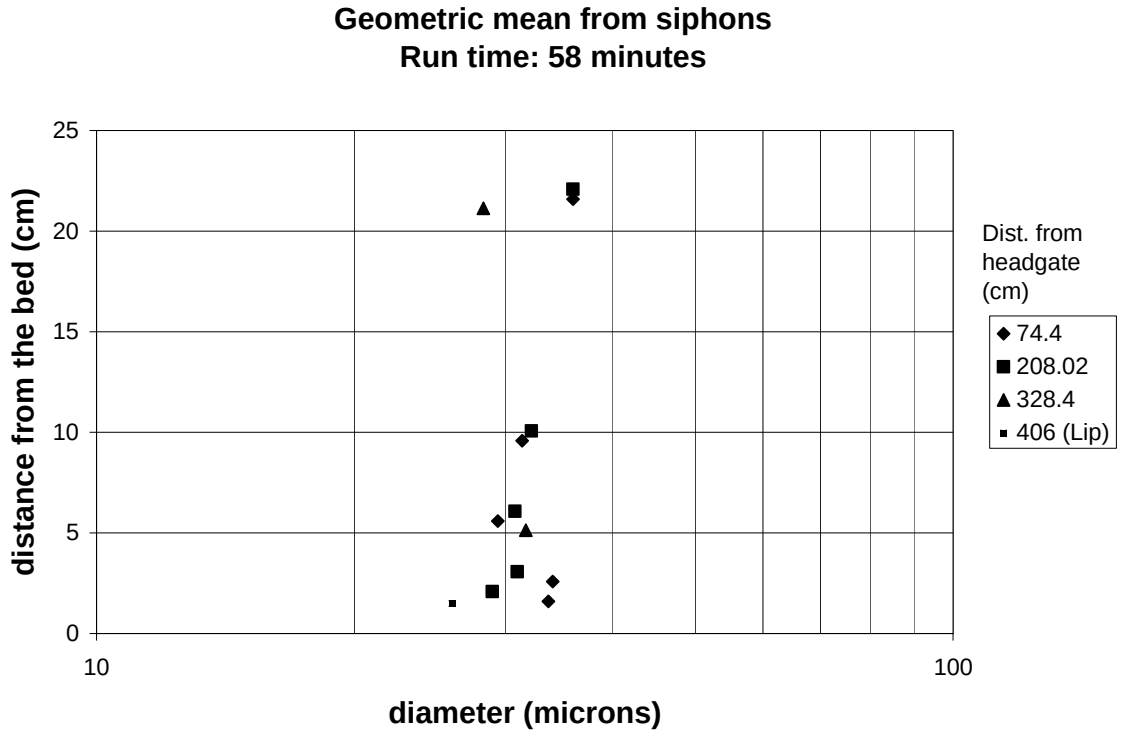


**Figure 12.**

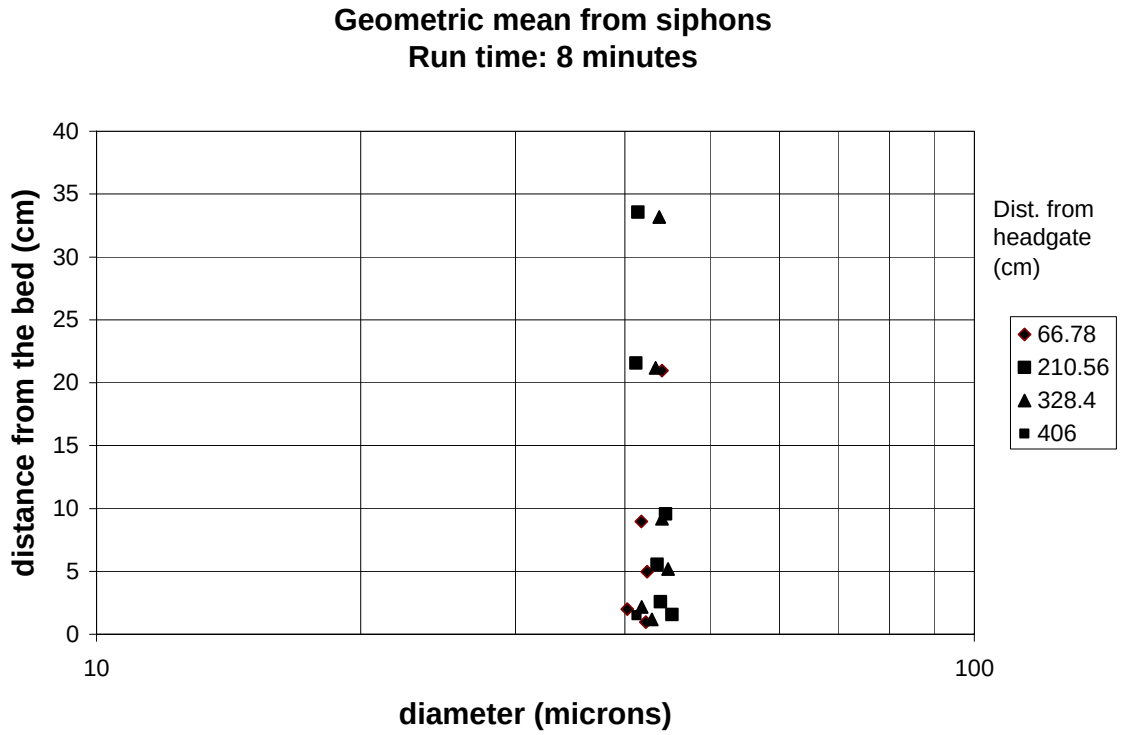


**Figure 13.**

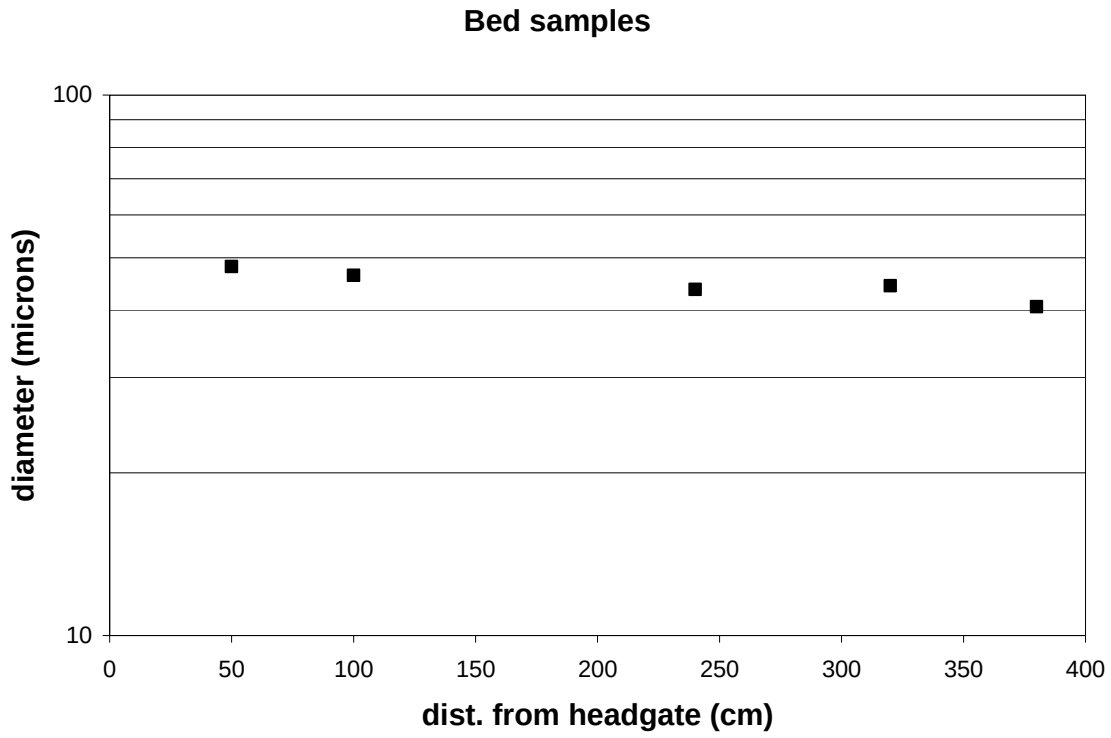


**Figure 14.**

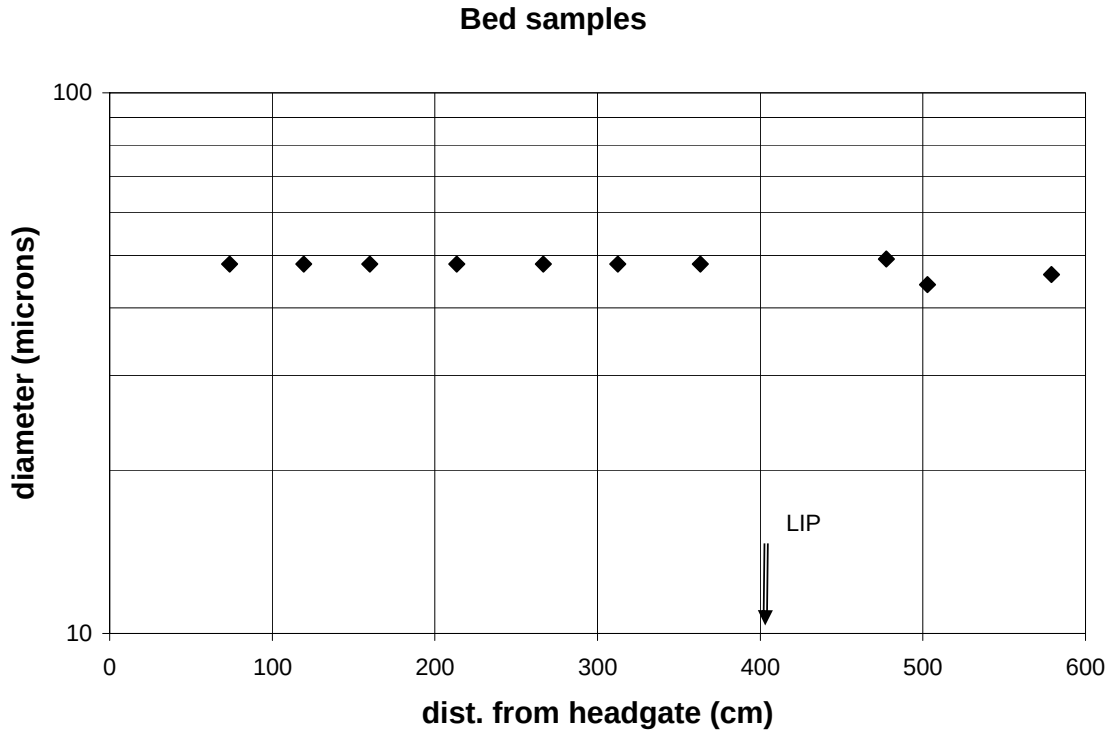


**Figure 15.**

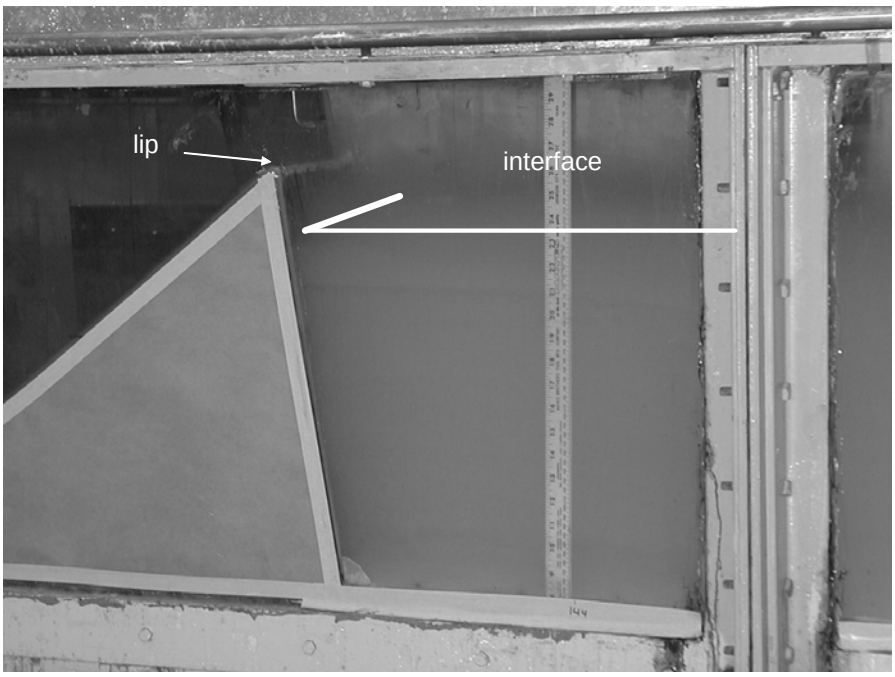


**Figure 16.**

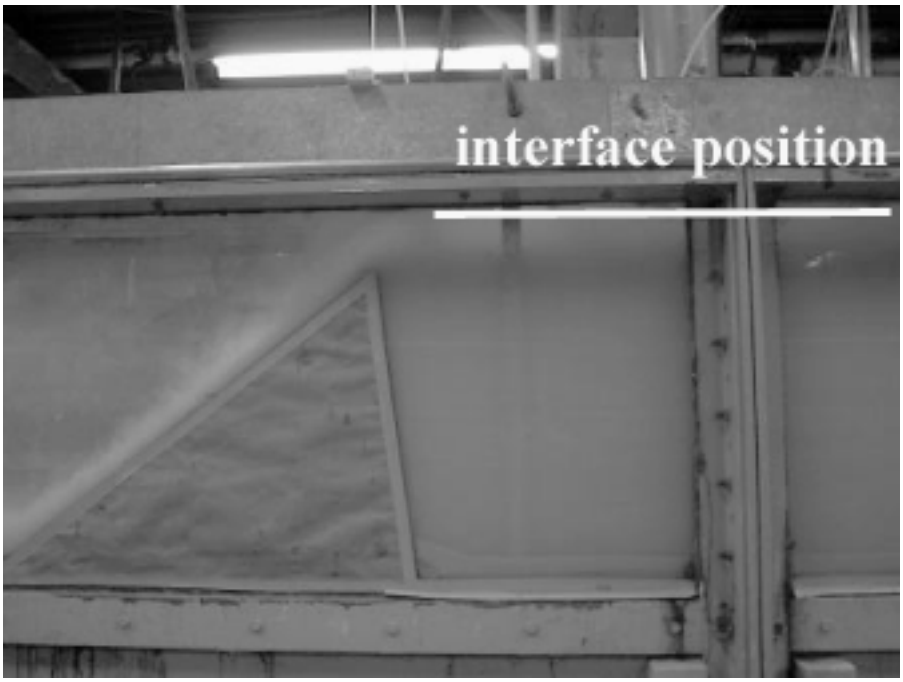


**Figure 17.**

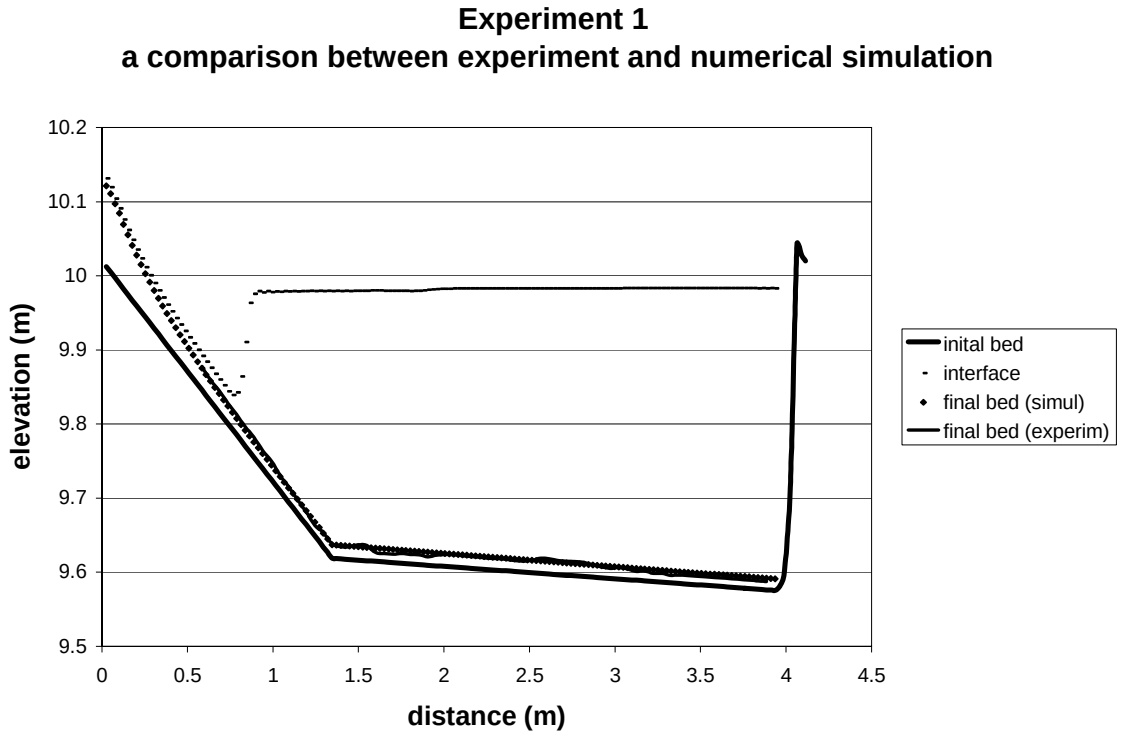


**Figure 18.**

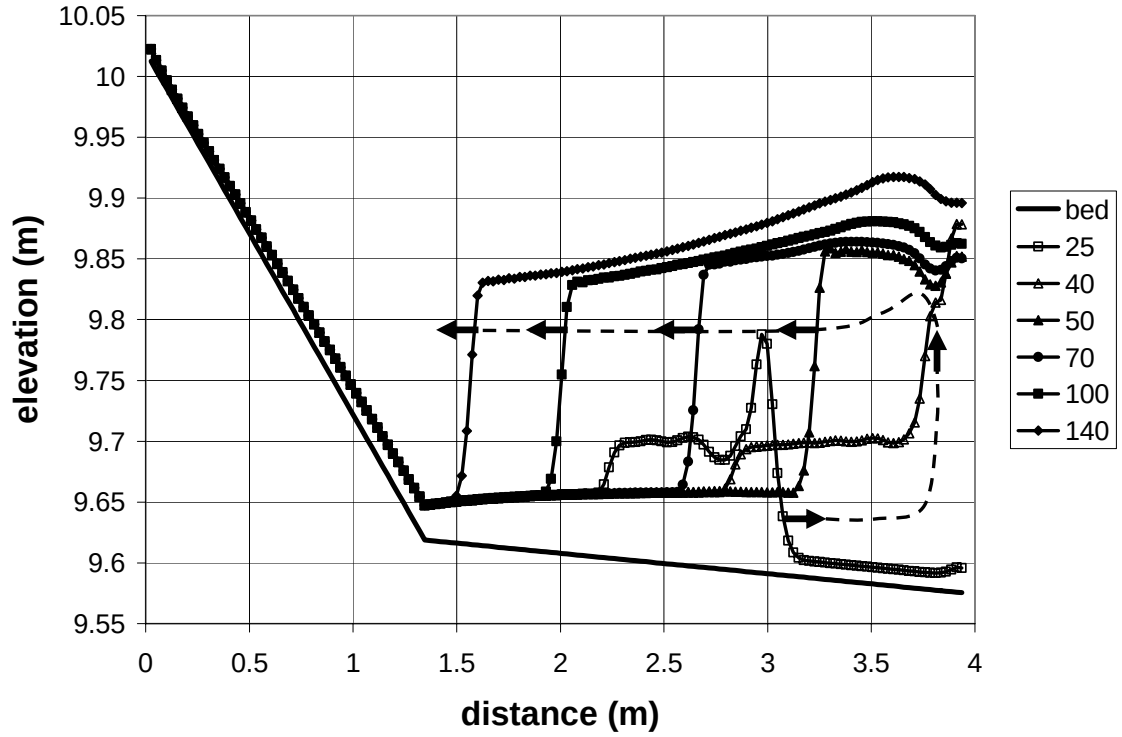


**Figure 19.**

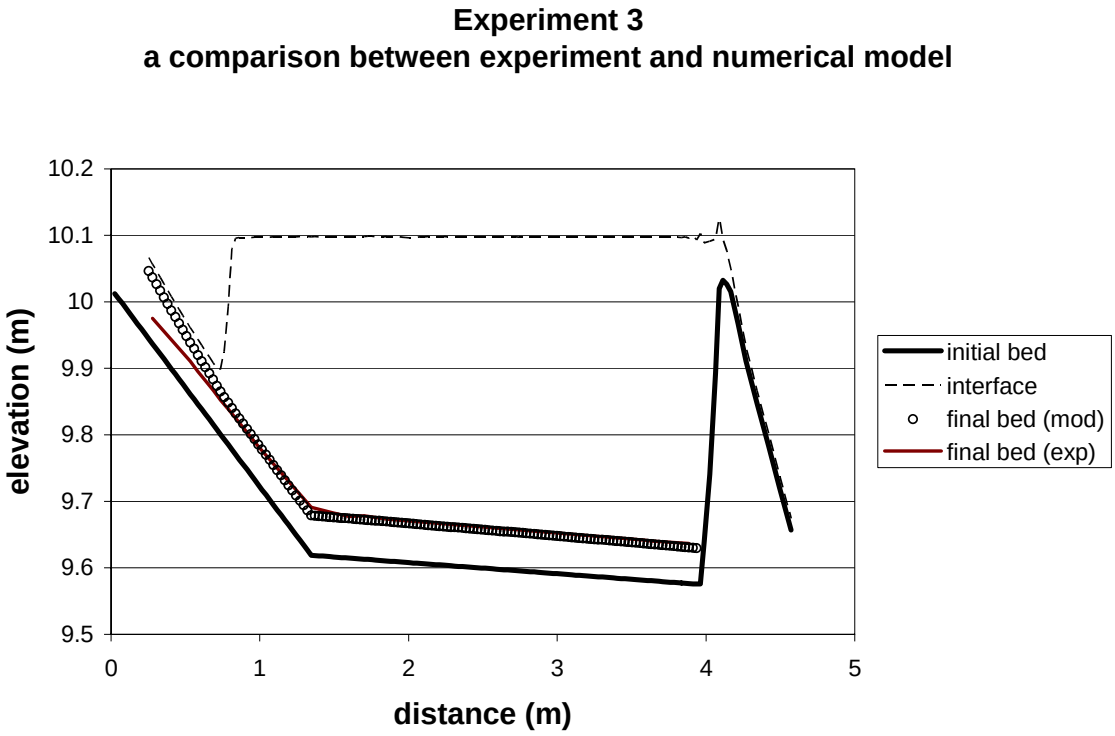


**Figure 20.**

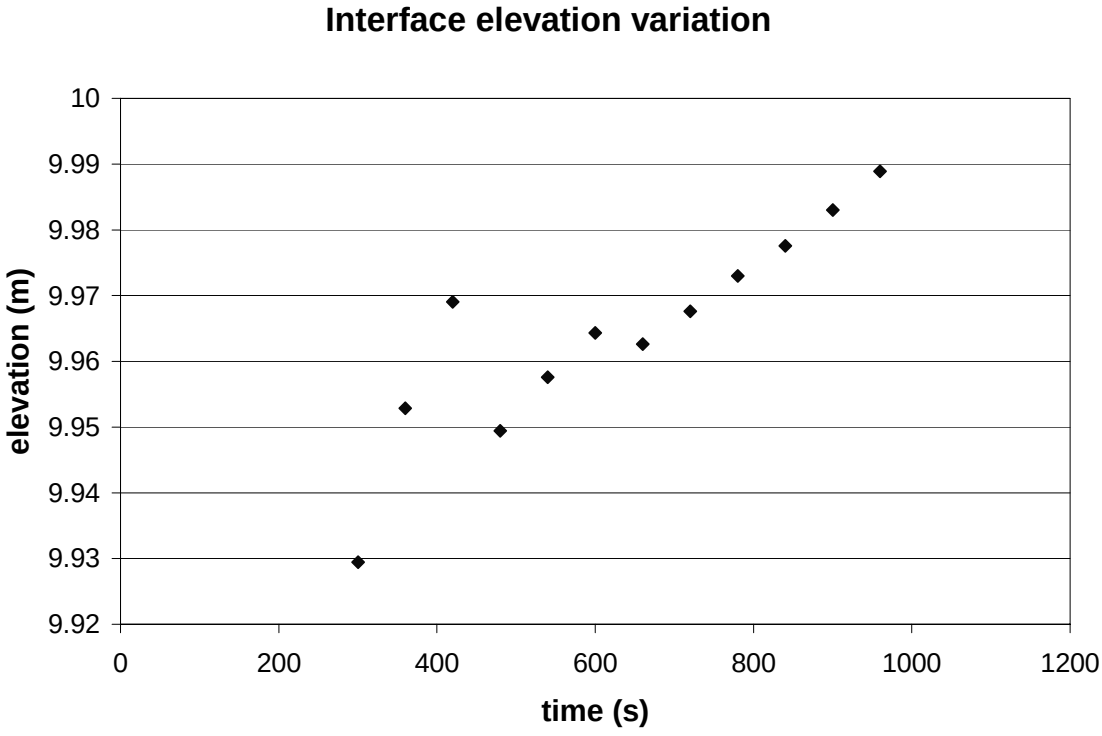


**Figure 21 a.**

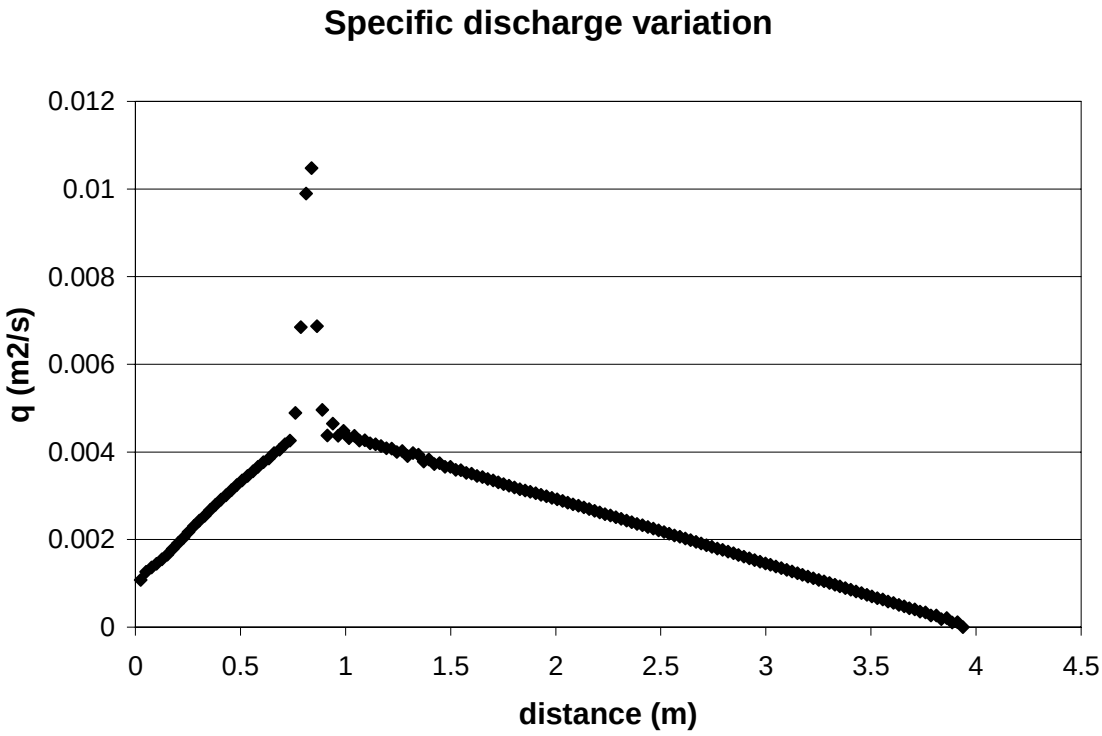


**Figure 21 b**

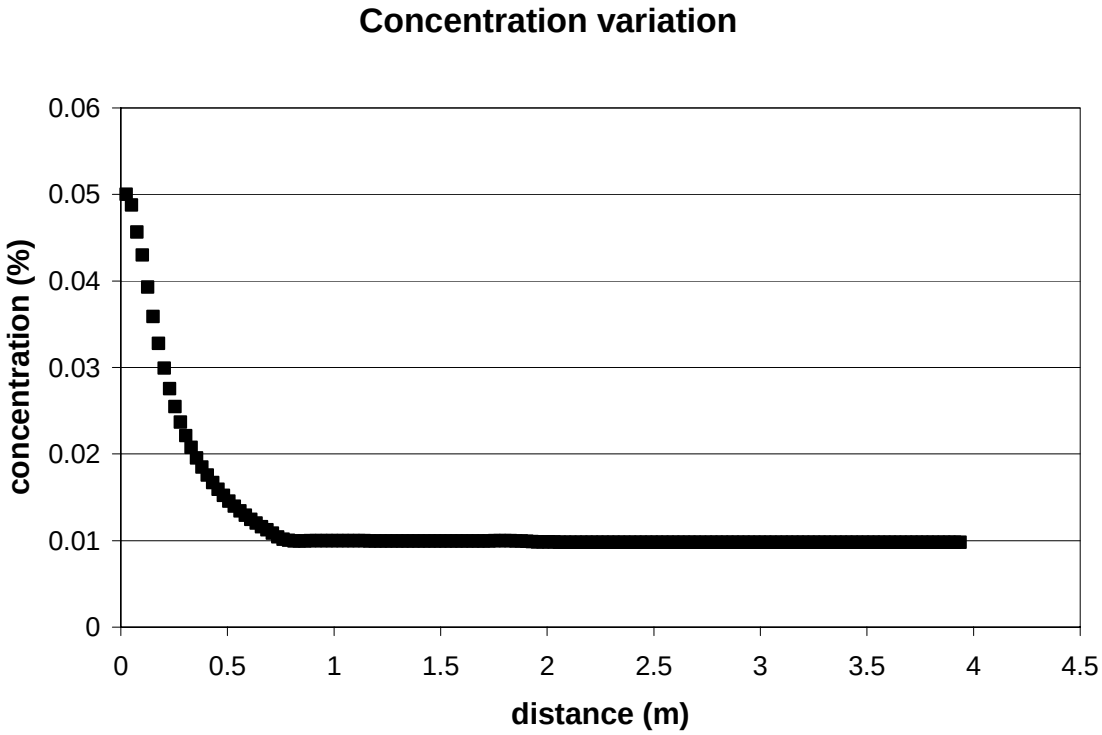


**Figure 21 c**

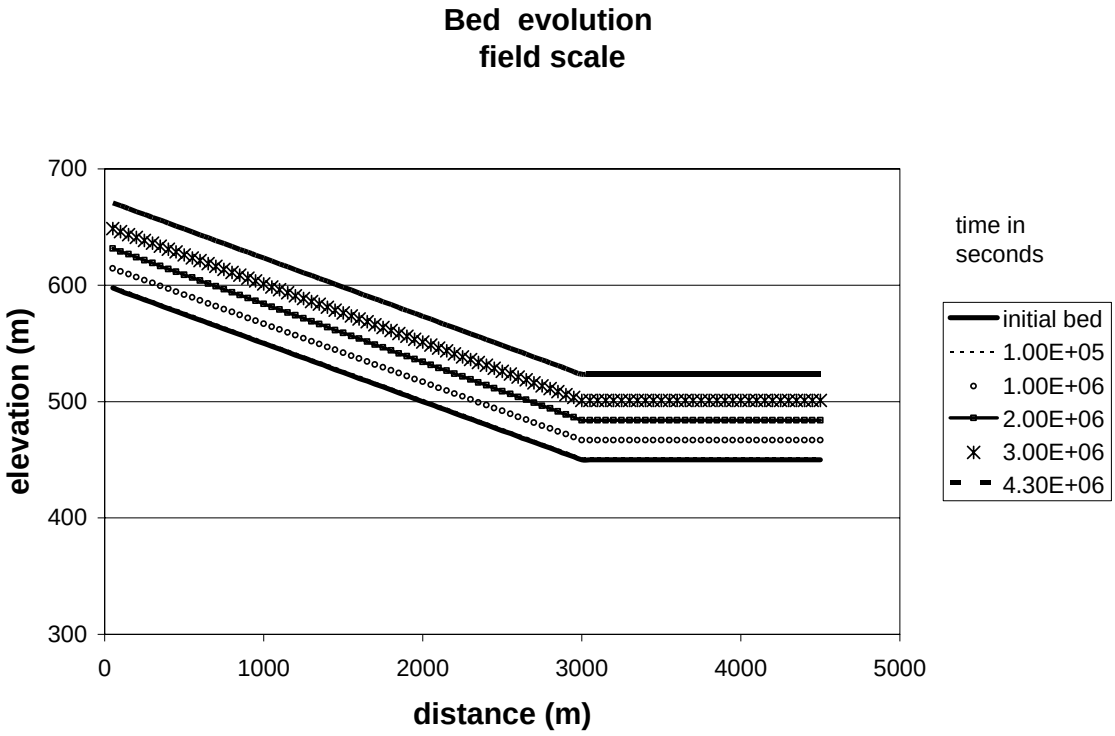


**Figure 22 a**

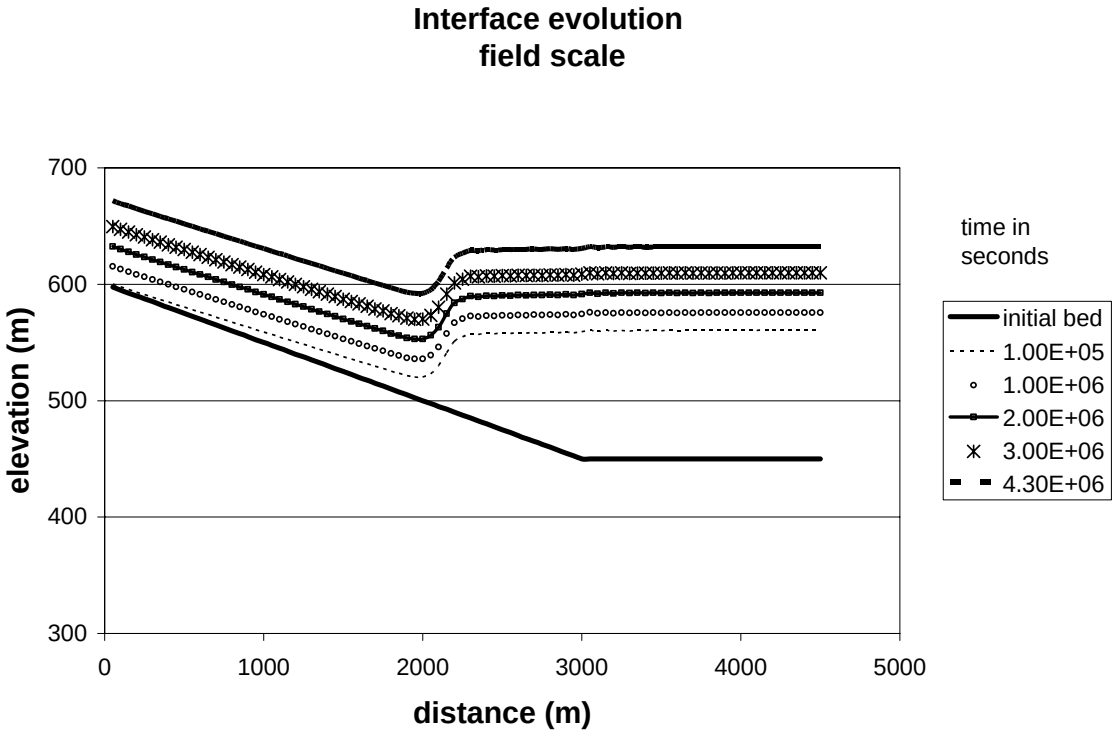


**Figure 22 b**

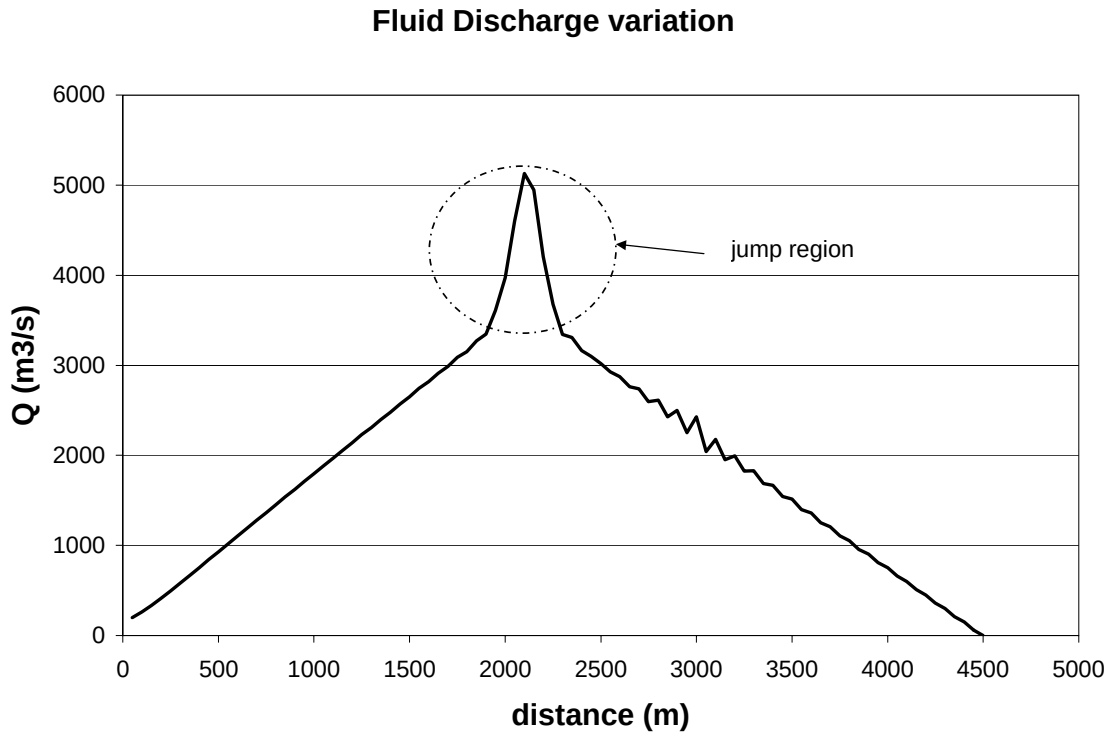


**Figure 22 c**

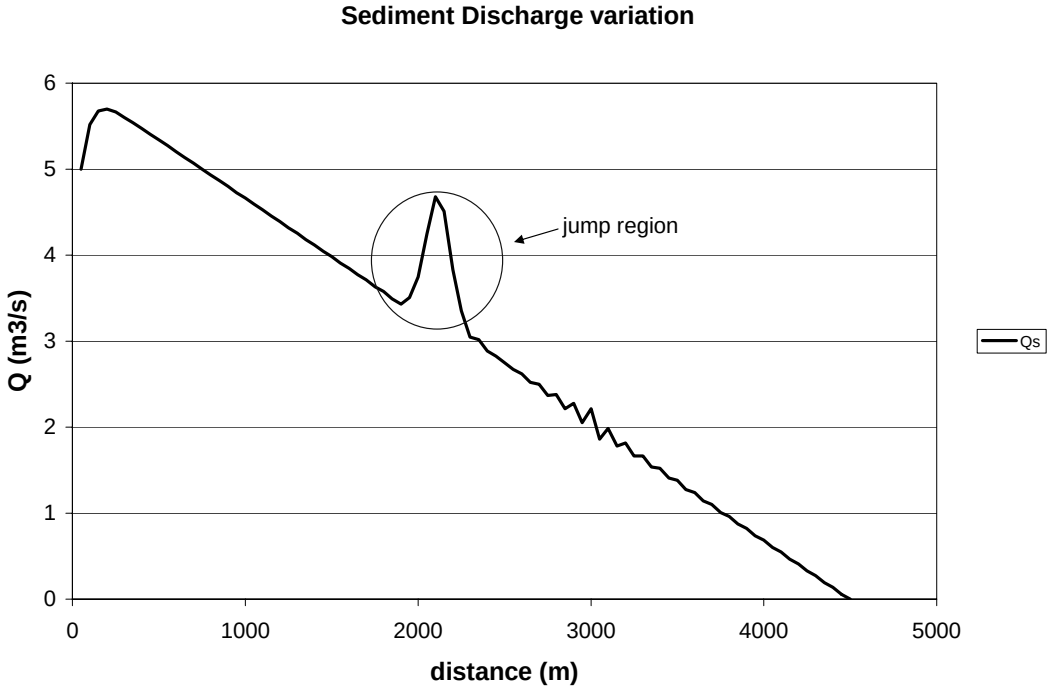


**Figure 22d**

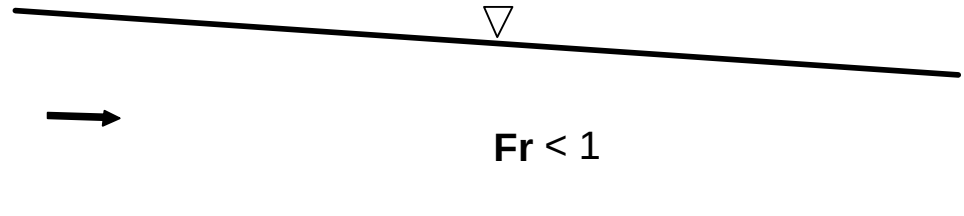


**Figure 23a**

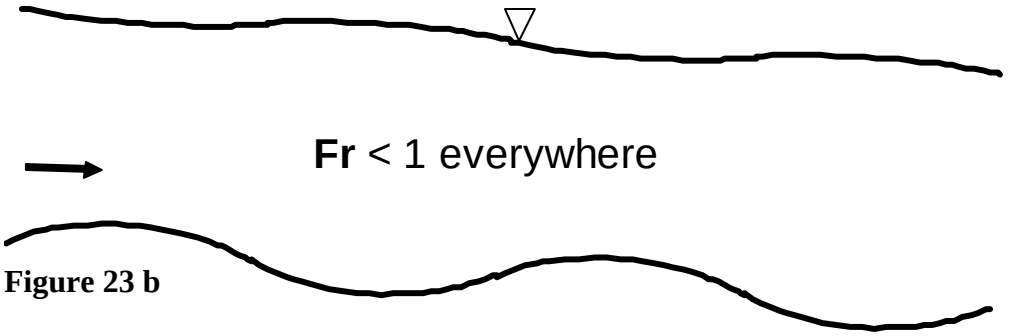


**Figure 23 b**

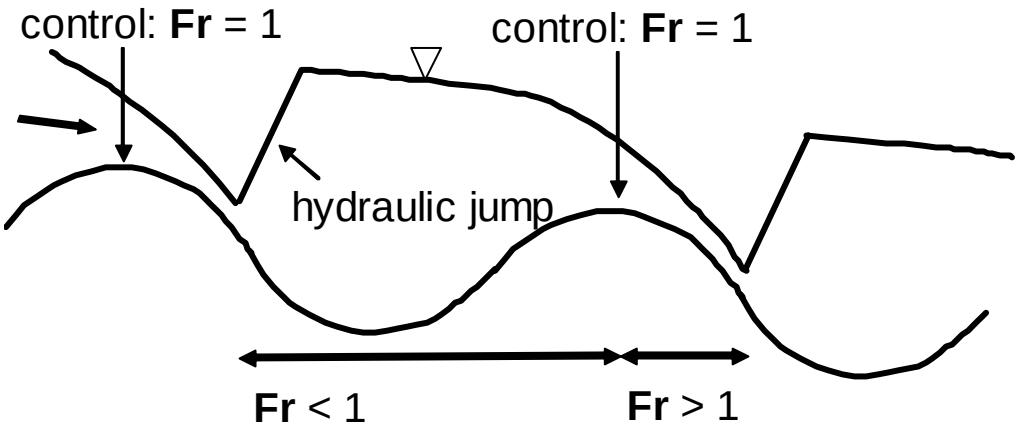


**Figure 23c**

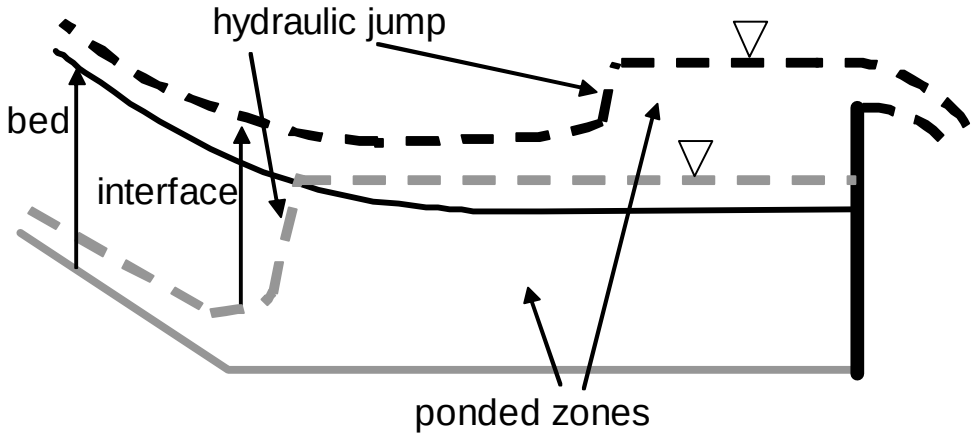


**Figure 24.**

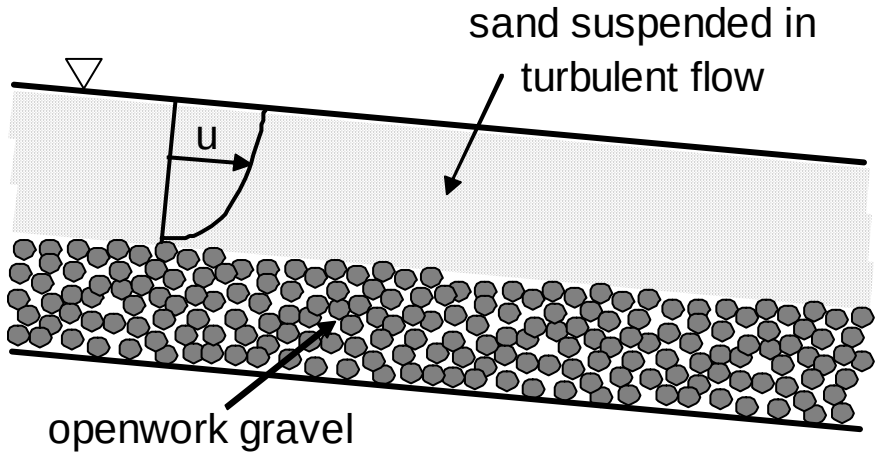


**Figure 25a**

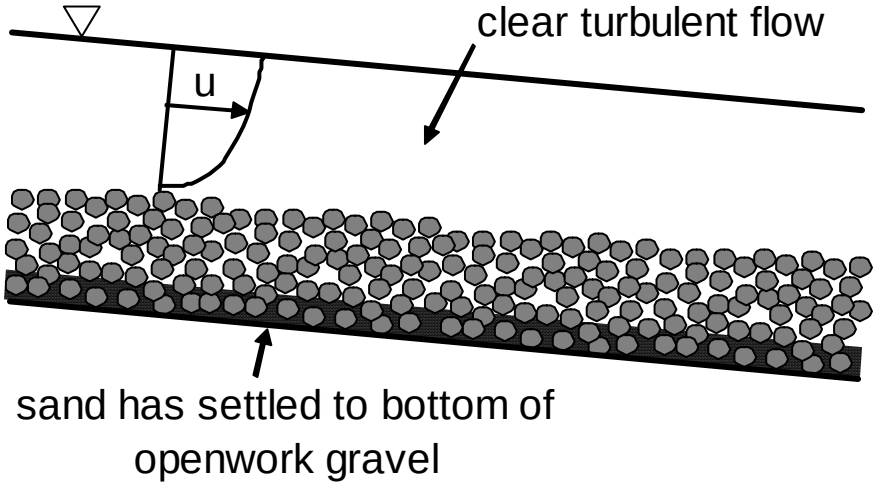


**Figure 25 b**

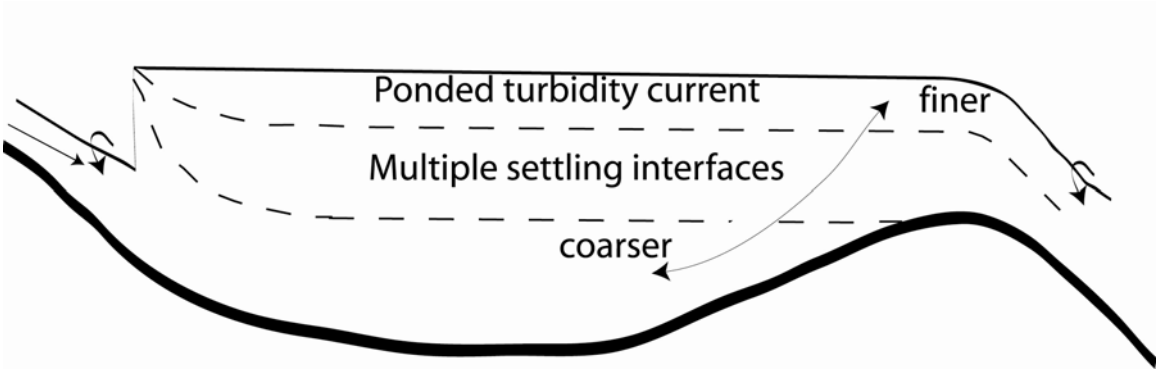


**Figure 26.**

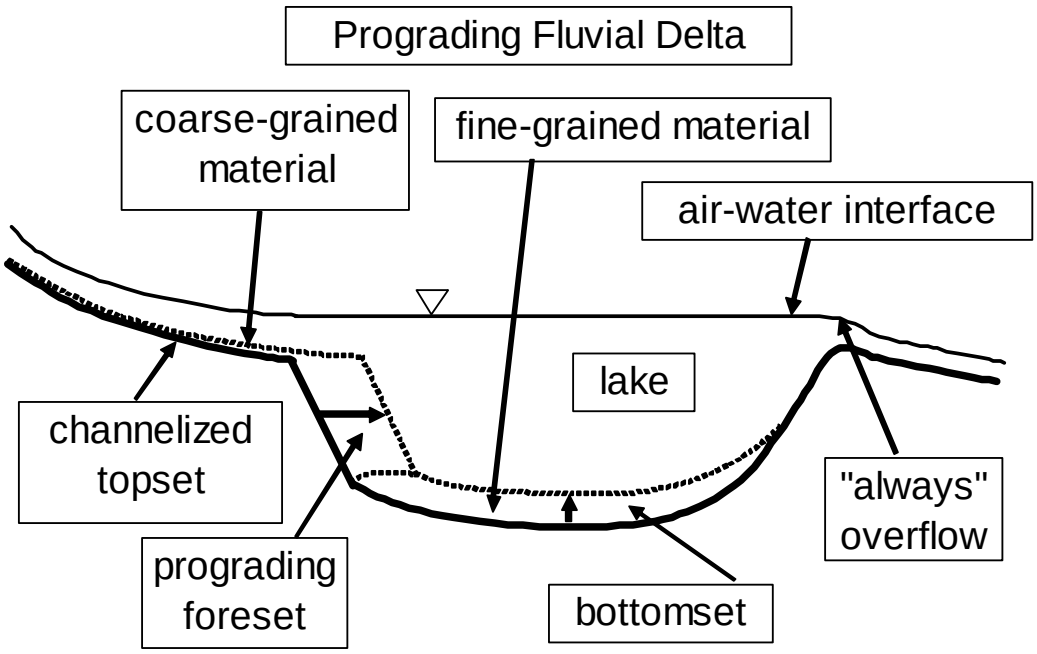


**Figure 27 a**

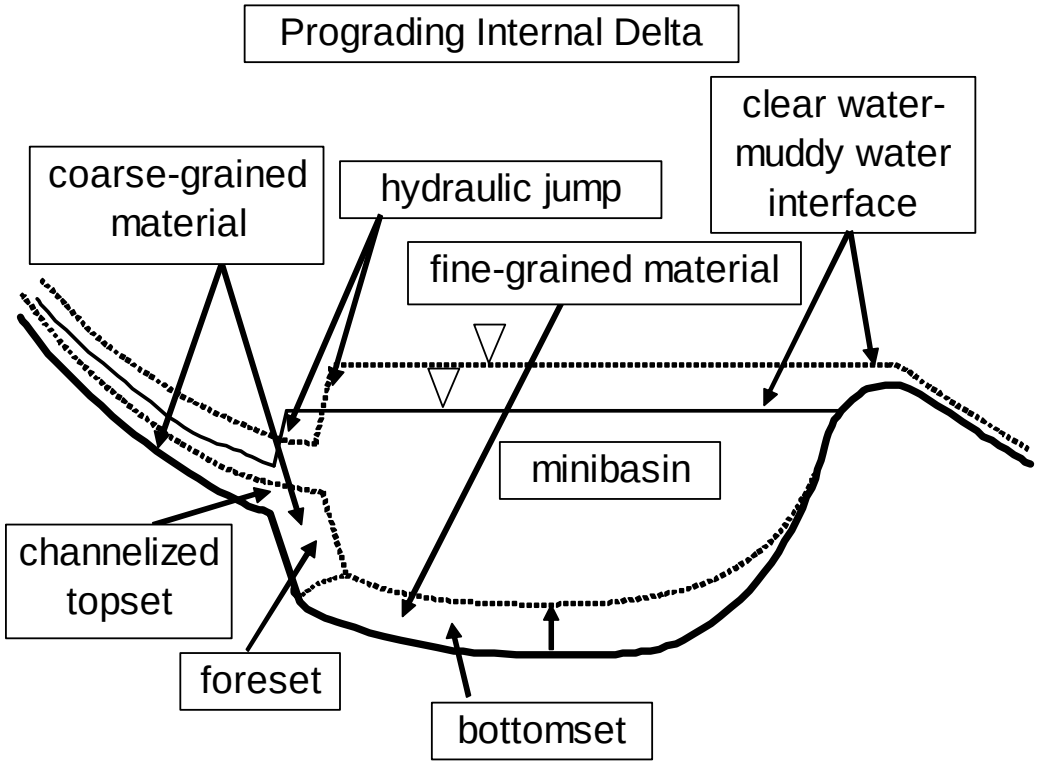


**Figure 27 b**